

# The ~1000-years BP explosive eruption of Caldeira Volcano (Faial, Azores): the first stage of incremental caldera formation

Adriano Pimentel<sup>1,2</sup> · José Pacheco<sup>2</sup> · Stephen Self<sup>3,4</sup>

Received: 29 December 2014 / Accepted: 8 April 2015  
© Springer-Verlag Berlin Heidelberg 2015

**Abstract** The ~1000-years BP eruption of Caldeira Volcano (Faial Island) was one of the last major explosive events recorded in the Azores. It produced a complex succession of pyroclastic deposits, known as the C11, divided into three members. At the base is the Brejo Member, a sequence of fine- to coarse-grained parallel-bedded ash layers found in the NW sector of the island. The middle part corresponds to the Inverno Member, a coarse-grained massive pumice fall deposit, restricted to the north flank of Caldeira Volcano. The top is dominated by the Cedros Member which includes massive to diffuse-stratified lapilli-ash and lithic breccias, exposed along the north and east flanks of the volcano. A minimum bulk volume of at least  $0.22 \text{ km}^3$  ( $>0.1 \text{ km}^3$  dense rock equivalent (DRE)) is estimated for the C11 eruption, although a large portion may have been deposited offshore. The juvenile products are trachytic (59 wt%  $\text{SiO}_2$ ) with a homogenous whole-rock composition and mineral assemblage throughout the pyroclastic succession. However, petrographic and

groundmass glass analyses indicate magma mingling/mixing processes between two trachytic batches. The C11 eruption history is divided into three phases (following the member division) with distinct eruptive styles: (1) an initial phreatomagmatic phase caused by rising magma ( $\sim 950^\circ \text{C}$ ) encountering a crater pond or aquifer, (2) a fall-dominated phase which established a sub-Plinian column up to 14 km high (mass eruption rate (MER) of  $1.2 \times 10^7 \text{ kg/s}$ ) and (3) prolonged pyroclastic fountaining and sustained quasi-steady pyroclastic density current generation followed by summit collapse. The C11 eruption is interpreted as the first stage in the formation of an incremental caldera. This study provides valuable insights for a better understanding of small but complex explosive eruptions and their impact on ocean islands.

**Keywords** Explosive eruption · Phreatomagmatism · Ignimbrite · Summit collapse · Magma mingling/mixing · Faial

Editorial responsibility: G. Giordano

**Electronic supplementary material** The online version of this article (doi:10.1007/s00445-015-0930-2) contains supplementary material, which is available to authorized users.

✉ Adriano Pimentel  
adriano.hg.pimentel@azores.gov.pt

<sup>1</sup> Centro de Informação e Vigilância Sismovulcânica dos Açores, 9501-801 Ponta Delgada, Azores, Portugal

<sup>2</sup> Centro de Vulcanologia e Avaliação de Riscos Geológicos, University of the Azores, 9501-801 Ponta Delgada, Azores, Portugal

<sup>3</sup> Department of Environment, Earth and Ecosystems, The Open University, Walton Hall, Milton Keynes MK7 6AA, UK

<sup>4</sup> Department of Earth and Planetary Science, University of California, Berkeley, CA 94720, USA

## Introduction

Explosive volcanic eruptions are one of the most destructive natural events that can threaten human society and affect the climate. Such eruptions produce sustained columns that are dispersed by the wind, sometimes for hundreds of kilometres, forming fall deposits and/or unstable columns that can collapse and generate pyroclastic density currents (PDCs). The latter may flow for several tens of kilometres and sometimes deposit ignimbrites many tens to hundreds of metres thick (e.g. Cas and Wright 1987; Branney and Kokelaar 2002; Sulpizio and Dellino 2008).

Highly explosive eruptions are often associated with caldera-forming events (CFEs). Deposits of large volume CFEs are rare in the Earth's geological record (Mason et al.

2004; Self 2006), but intermediate to small volume explosive eruptions occur much more frequently and, therefore, pose a higher risk to surrounding populations. In historical times, CFEs have caused several tens of thousands of fatalities and severe consequences to global climate (Rampino and Self 1982; Tanguy et al. 1998), as seen during the Pinatubo AD 1991 eruption, Philippines (Scott et al. 1996).

The Azores archipelago has an extensive record of explosive eruptions spread over at least four of the nine constituent islands. They typically occur at central volcanoes with incrementally formed calderas, where intermediate to small volume eruptions recur (e.g. Walker 1984; Guest et al. 1999; Wallenstein 1999; Pacheco 2001; Queiroz et al. 2008; Gertisser et al. 2010). Among these, the Fogo A, the Fogo AD 1563 (Walker and Croasdale 1971), the Furnas AD 1630 (Cole et al. 1995) and the Lajes-Angra Ignimbrite (Self 1976) are some of the best known examples.

One of the last major explosive eruptions in the Azores, the C11 eruption, occurred ~1000-years BP (Pacheco 2001) on Faial Island. It was the most complex and prominent eruption of Caldeira Volcano and produced a sequence of ash layers followed by a pumice fall deposit and, during the final phase, an ignimbrite sheet and lithic breccias. However, due to the small size of the island, much of the erupted material was probably deposited offshore. Pacheco (2001) estimated that the total bulk volume of the eruption may have been  $>0.7 \text{ km}^3$ , making it the largest eruption in Faial during the last 16 kyr.

The C11 deposit provides a good opportunity to better understand the eruptive dynamics of complex explosive eruptions and their impact on small ocean islands. Here, individual lithofacies and their associations are described, together with analyses of grain size, componentry, morphology and chemical composition of juvenile products. The aims are to reconstruct the eruption history of C11 and to obtain an accurate understanding of the eruptive mechanisms. These insights are of particular importance for a realistic assessment of the impacts of future explosive eruptions on Faial or on other ocean islands vulnerable to this type of event.

## Geological setting and evolution of Faial

Faial Island, in the Azores archipelago, is located in the North Atlantic Ocean in a complex geodynamic setting resulting from the interaction between the triple junction of the North American, Eurasian and Nubian plates (Fig. 1a) and hotspot magmatism. State-of-the-art reviews can be found in Gente et al. (2003), Vogt and Jung (2004), Georgen and Sankar (2010) and Trippanera et al. (2014).

Faial became emergent during the Pleistocene and was built by central and fissure volcanism. It is composed of the central volcanoes of Ribeirinha and Caldeira and the fissure

systems of Horta Platform and Capelo Peninsula (Fig. 1b, c; Serralheiro et al. 1989; Madeira 1998; Pacheco 2001; Madeira and Brum da Silveira 2003). The oldest unit of Faial is Ribeirinha Volcano ( $>850 \text{ ka}$ ; Hildenbrand et al. 2012), an extinct shield volcano composed of basaltic/benmoreitic lavas known as the Ribeirinha Volcanic Complex. Volcanic activity ceased ~580 ka (Serralheiro et al. 1989; Madeira 1998) and the shield is now dissected by the Pedro Miguel Graben.

The central portion of the island is dominated by Caldeira Volcano (1043 m asl), a central volcano truncated by a 2-km-wide and ~370-m-deep summit caldera. Volcanic activity started  $>440 \text{ ka}$  (Baubron 1981, in Chovelon 1982) and has continued until the present. The products of Caldeira Volcano constitute the Cedros Volcanic Complex which is divided into two groups (Serralheiro et al. 1989; Madeira 1998; Pacheco 2001). The Lower Group ( $>16 \text{ ka}$ ) is formed by basaltic/benmoreitic lavas and two trachytic domes, while the Upper Group ( $<16 \text{ ka}$ ) consists of trachytic pyroclastic deposits from 14 explosive eruptions (named C1 to C14; Pacheco 2001; Fig. 1c). The deposits of C1 to C10 and C12 eruptions are small volume and constituted by pumice and/or ash fall deposits and minor PDC deposits, while C13 and C14 events are recorded by a scoria cone and a phreatic explosion (AD 1958), respectively. The deposit of the C11 eruption is clearly distinct from the others of the Upper Group as it is the only that comprises an extensive ignimbrite sheet and lithic breccias.

The Horta Platform fissure system consists of a basaltic lava field with several scoria cones and a tuff cone, included in the Almoxarife Formation. Its eruptive period is poorly constrained and spans from  $30 \pm 20 \text{ ka}$  (Féraud et al. 1980) to ~11 ka (Serralheiro et al. 1989; Madeira 1998).

The Capelo Peninsula fissure system is formed by a WNW-ESE trending ridge of scoria cones and a few tuff cones that produced basaltic/hawaiitic lavas. These products constitute the Holocene Capelo Formation, the youngest unit on Faial (Serralheiro et al. 1989; Madeira 1998; Di Chiara et al. 2014), and it includes those of two historical eruptions: Cabeço do Fogo AD 1672–1673 and Capelinhos AD 1957–1958.

Two major fault systems occur on Faial (Fig. 1b). The WNW-ESE system is well expressed by the faults of Pedro Miguel Graben, which cross the Caldeira Volcano, and controls the en échelon alignment of scoria cones on Capelo Peninsula. A secondary conjugate NNW-SSE fault system occurs in the northern side of the island (Serralheiro et al. 1989; Madeira 1998; Madeira and Brum da Silveira 2003; Trippanera et al. 2014).

## Methodology

The C11 deposit was studied in detail by mapping and lithofacies analysis. More than 150 stratigraphic sections were reconstructed (Fig. 2); each was thoroughly documented and

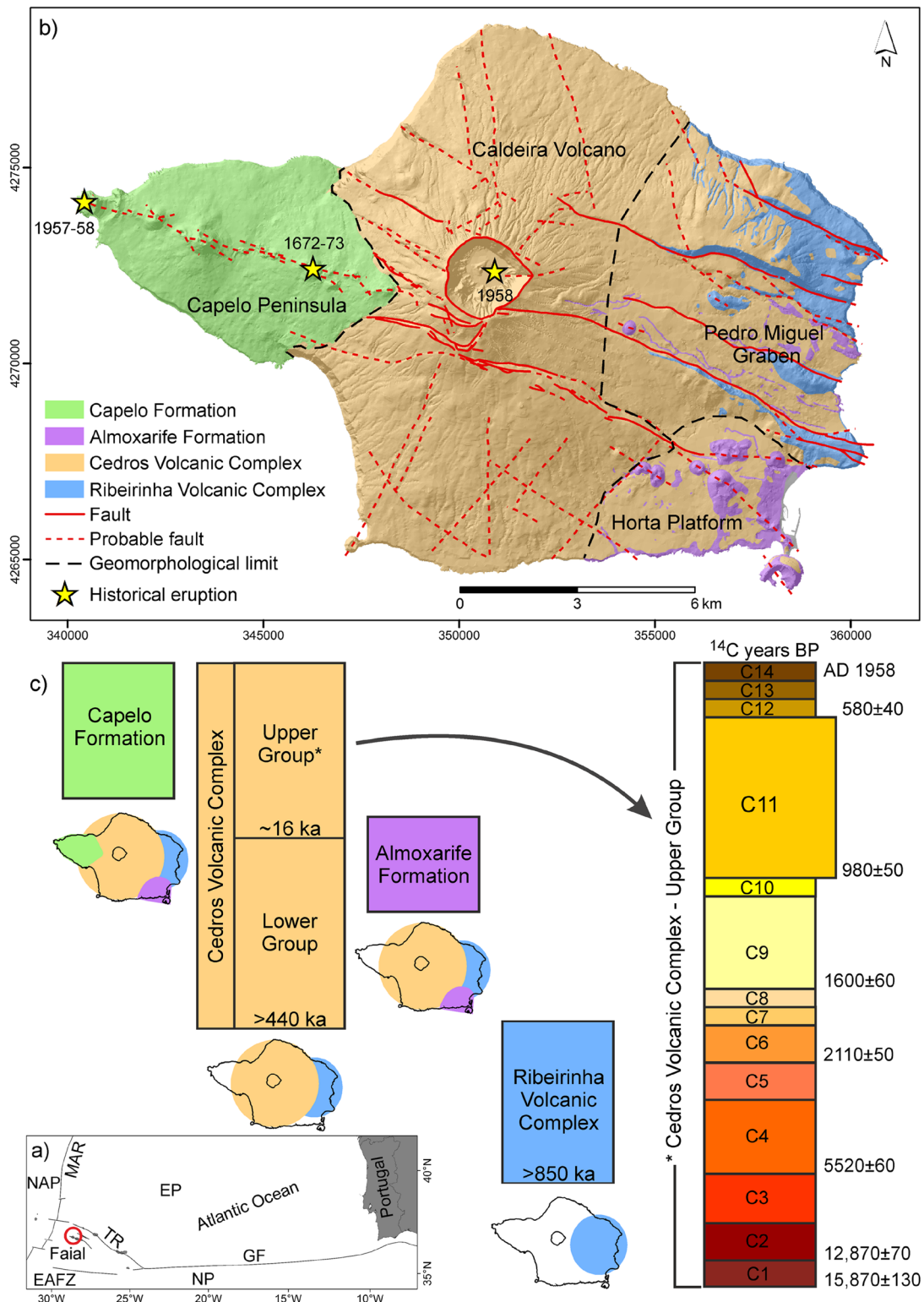


**Fig. 1** **a** Geological setting of the Azores. *NAP* North American Plate, *EP* Eurasian Plate, *NP* Nubian Plate, *MAR* Mid-Atlantic Ridge, *TR* Terceira Rift, *EAFZ* East Azores Fracture Zone, *GF* Gloria Fault. **b** Simplified geological map of Faial Island (modified from Serralheiro et al.

1989); UTM coordinates, zone 26S. **c** Stratigraphic scheme and evolution of Faial Island (adapted from Pacheco 2001). In the Cedros Volcanic Complex Upper Group scheme, the thickness, not to scale, shows the relative volumetric expression among deposits

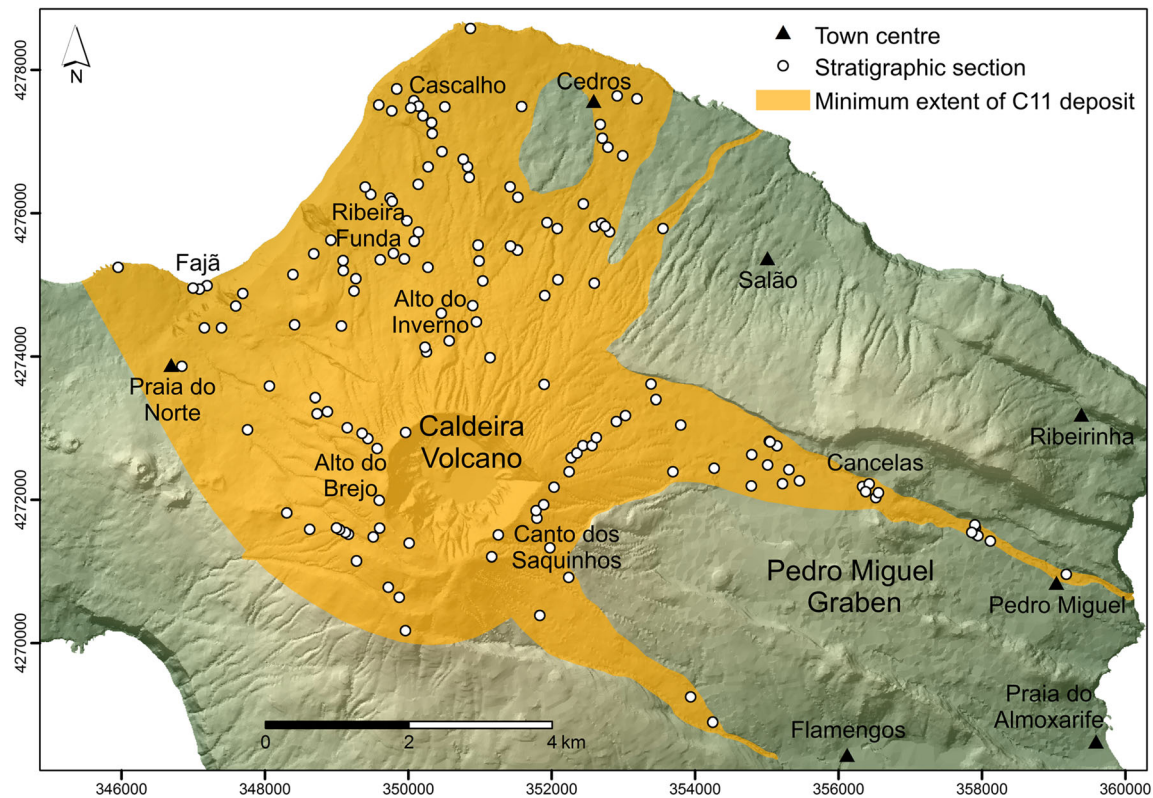


**Fig. 2** Map of the minimum extent of the C11 deposit on land, including fall and ignimbrite deposits, and documented stratigraphic sections. Main locality names referred in the text are shown; UTM coordinates, zone 26S

palaeosols and/or erosion surfaces were used to delimit the deposit. The maximum clast size (pumice and lithic clasts) of each member was determined by averaging the length of the major axis of the three largest clasts.

Lithofacies analysis was used to obtain an overall understanding of the eruptive and depositional processes. This approach has been widely applied on complex pyroclastic successions and ignimbrite sheets (e.g. Sohn and Chough 1989; Allen and Cas 1998; Brown and Branney 2004; Brown et al. 2007; Sulpizio et al. 2007, 2010). Lithofacies terminologies and abbreviations (Table 1) follow Branney and Kokelaar (2002) and Sulpizio et al. (2007). The nomenclature for bed thickness, grain size and sorting was adopted from Sohn and Chough (1989).

Fieldwork was coupled with grain size and component analyses (Table 2), following the methodology of Cas and Wright (1987). The samples were sieved at  $0.5 \phi$  intervals from  $-6$  to  $5 \phi$  (64–0.032 mm) and separated into three main components: pumices, lithics and crystals. Details on the methods are given in the Appendix.

The morphology of juvenile ash particles (in the size range of 4 to 5  $\phi$ ) was examined using scanning electron microscope (SEM) images, in order to establish the main mechanisms of magma fragmentation, following Dellino and La Volpe (1995; see Appendix).

Petrographic and modal analyses of thin sections were complemented with whole-rock major and trace elements

analyses (ESM Table A.2) performed by fusion inductively coupled plasma (FUS-ICP) and inductively coupled plasma mass spectrometry (ICP-MS), at the Activation Laboratories

**Table 1** Lithofacies abbreviation key (modified from Branney and Kokelaar 2002; Sulpizio et al. 2007)

Key	Lithofacies terms
//bA	Parallel-bedded ash
mA	Massive ash
mCA	Massive coarse ash
sA	Stratified ash
mAacc	Massive ash with accretionary lapilli
mpL	Massive pumice lapilli
mpLB	Massive pumice lapilli-block
mLA	Massive lapilli-ash
dbLA	Diffuse-bedded lapilli-ash
dsLA	Diffuse-stratified lapilli-ash
sLA	Stratified lapilli-ash
lBr	Lithic breccia
mlBr	Massive lithic breccia
dblBr	Diffuse-bedded lithic breccia
pLBlens	Lenses of pumice-rich lapilli-block
lLBlens	Lenses of lithic-rich lapilli-block
lpip	Fines-poor lithic-rich pipe

**Table 2** Grain size parameters and components of representative samples and correspondence with the C11 members (after Inman 1952; Folk and Ward 1957; see Figs. 4, 7 and 10 for location and Table 1 for lithofacies key)

Member	Sample	Lithofacies	$Md\phi$	$\sigma\phi$	$Mz$	$\sigma I$	P (wt%)	L (wt%)	C (wt%)	NA (wt%)
Brejo	FAYS73-1	mA	1.55	2.10	1.70	2.03	—	—	—	—
Brejo	FAYS73-2	mA	2.78	2.22	2.40	2.20	—	—	—	—
Brejo	FAYS93-1	mCA	−0.93	1.17	−0.88	1.19	—	—	—	—
Brejo	FAYS93-2	mCA	0.05	1.39	−0.09	1.47	38.5	39.4	1.9	20.1
Brejo	FAYS97-1	mCA	−0.07	1.19	−0.03	1.25	7.0	69.7	4.6	18.7
Brejo	FAYS97-2	mA	2.42	1.84	2.40	1.69	—	—	—	—
Brejo	FAYS123-1	mA	4.18	1.81	3.44	1.35	—	—	—	—
Brejo	FAYS123-2	mCA	−0.54	1.19	−0.40	1.25	—	—	—	—
Brejo	FAYS123-3	mA	4.01	2.37	2.98	1.74	—	—	—	—
Brejo	FAYS123-4	mpL	−1.28	1.21	−1.15	1.30	—	—	—	—
Brejo	FAYS123-5	mA	3.90	1.36	3.52	1.23	—	—	—	—
Brejo	FAYS123-6	mCA	0.15	1.18	0.15	1.27	—	—	—	—
Inverno	FAYS73-4	mpLB	−4.00	1.19	−3.85	1.39	70.3	26.4	0.7	2.7
Cedros	FAYS7-3	mLA	0.99	2.45	1.19	2.27	7.6	36.1	6.4	49.9
Cedros	FAYS12-4	mLA	1.88	2.03	2.03	1.94	12.5	16.6	2.6	68.4
Cedros	FAYS12-5	mLA	0.86	2.58	0.89	2.45	3.9	41.0	7.4	47.7
Cedros	FAYS46-3	mLA	−0.50	2.45	−0.48	2.43	17.2	49.5	5.5	27.9
Cedros	FAYS46-4	mLA	−0.25	2.26	−0.26	2.22	16.7	47.5	6.3	29.5
Cedros	FAYS48-2	mLA	−0.17	2.81	−0.15	2.75	18.6	42.8	5.4	33.2
Cedros	FAYS52-1	mLA	1.04	2.75	1.16	2.58	8.8	36.2	4.5	50.6
Cedros	FAYS89-3	dbLA	0.82	3.19	0.83	2.87	14.6	34.2	3.6	47.5
Cedros	FAYS89-4	dbLA	1.66	3.13	1.39	2.76	12.2	25.5	3.4	58.9
Cedros	FAYS89-5	dbLA	1.99	2.79	1.76	2.71	16.1	18.5	2.5	62.9
Cedros	FAYS145-3	sLA	1.36	2.44	1.69	2.05	—	—	—	—
Cedros	FAYS30-1	mLA <sup>a</sup>	−0.78	2.58	−0.76	2.57	29.6	38.0	7.6	24.8

$Md\phi$  mean diameter,  $\sigma\phi$  graphic standard deviation or sorting,  $Mz$  graphic mean,  $\sigma I$  inclusive graphic standard deviation or sorting,  $P$  pumices,  $L$  lithics,  $C$  crystals,  $NA$  not analysed ash

<sup>a</sup> Corresponds to the pumiceous lapilli-ash matrix of the lithic breccia

Ltd., Ontario (Canada), and electron microprobe analyses of the mineral phases (ESM Table A.1) and groundmass glass (details in the Appendix).

### Stratigraphy of the C11 deposit

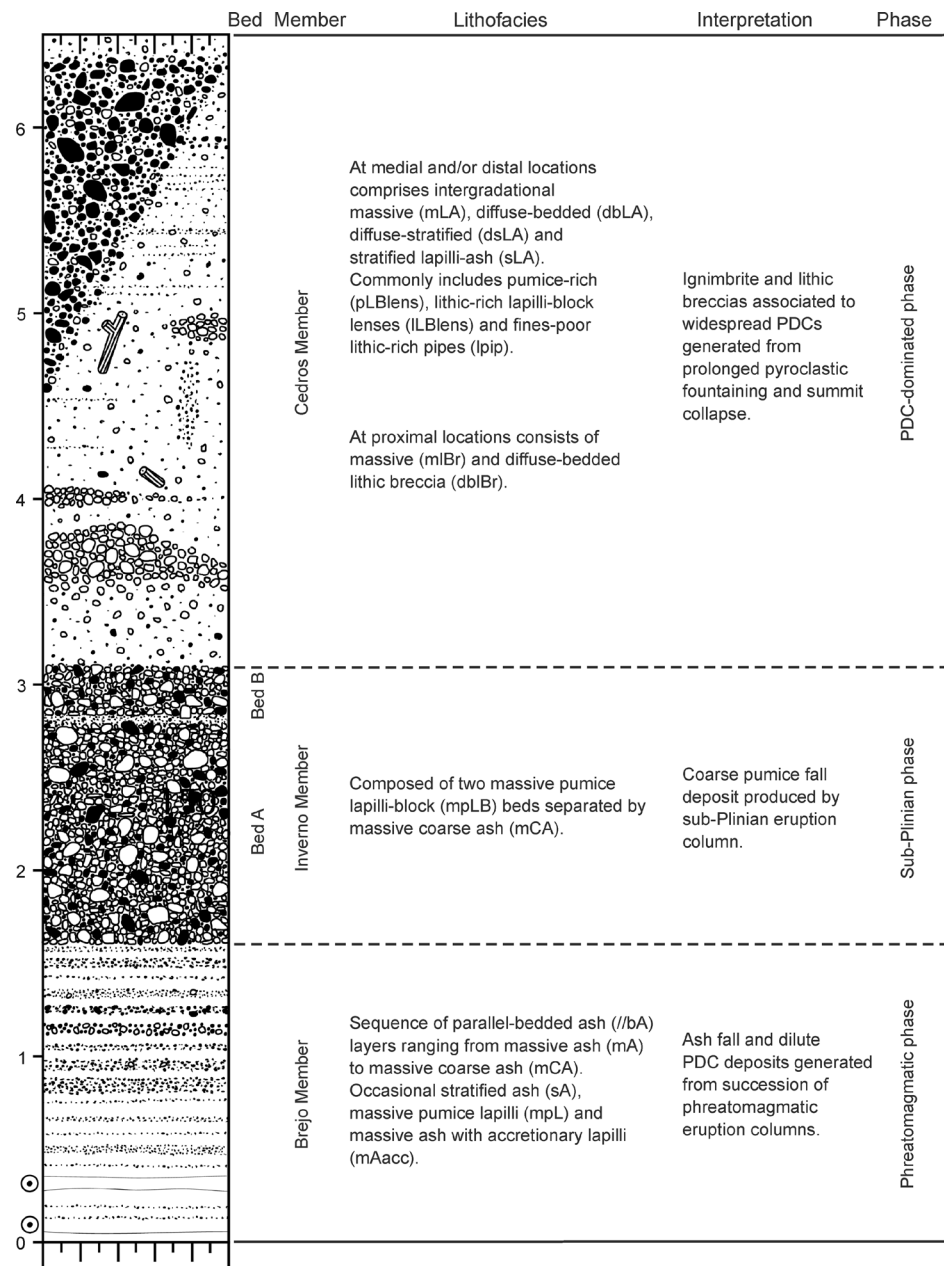
The C11 deposit ( $980 \pm 50$   $^{14}\text{C}$  years BP; Pacheco 2001) outcrops mainly on the north and west slopes of Caldeira Volcano and the northern margin of Pedro Miguel Graben (Fig. 2). In general, it is found above the C9 pumice fall deposit ( $1600 \pm 60$   $^{14}\text{C}$  years BP; Pacheco 2001) and occasionally overlies the inconspicuous C10 ash deposit. It is only partially concealed by the small volume C12 deposit ( $580 \pm 40$   $^{14}\text{C}$  years BP; Pacheco 2001), making it widely present at the surface. The C11 deposit varies in thickness from 0.15 to >14 m and comprises three members, defined by stratigraphic position and dominant lithofacies, that represent the three distinct phases of the eruption (Fig. 3).

At the base of the C11 pyroclastic succession is the Brejo Member (BM), which consists of a sequence of fine to coarse ash layers deposited on the NW sector of Faial. The middle part is the Inverno Member (IM), a coarse pumice fall deposit that outcrops on the north flank of the volcano. The top of the C11 is dominated by the Cedros Member (CM), composed of massive to diffuse-stratified ignimbrite and lithic breccias, emplaced on the slopes of the volcano and Pedro Miguel Graben. No significant discontinuities were found between the members, suggesting that the C11 deposit represents a single eruptive event with no major pauses. The three members will be fully described and interpreted in the next sections.

### Brejo Member

The BM comprises numerous parallel-bedded ash (//bA) layers and is well represented by outcrops at Alto do Brejo (type location FAYL123; Fig. 4), where it is >2.6 m thick. It

**Fig. 3** Composite stratigraphic section of the C11 pyroclastic succession with reference to the members and corresponding eruptive phases



shows a gradual transition from a lower part dominated by massive fine-grained ash beds (mA; Fig. 5a) to an upper part mainly composed of massive coarse-grained ash beds (mCA; Fig. 5b).

**Lithofacies** The mA to mCA beds range in thickness from very thin to thin (<1 to ~10 cm) and show well-defined parallel bedding. Some massive ash layers occasionally grade laterally into stratified ash (sA; Fig. 5c).

The mA beds (Mdφ 1 to 4.5) are composed of juvenile ash, occasionally containing accretionary lapilli (mAacc), mostly

ash pellets and some coated ash pellets, and moulds of small branches (Fig. 5d). Fine-ash particles are predominantly made up of juvenile glass shards, with subordinate lithic clasts and crystals. Juvenile ash particles exhibit variable morphologies under the SEM, including dense blocky clasts with stepped fractures (Fig. 5e), subrounded moss-like clasts (Fig. 5f), fused-shaped poorly vesicular clasts (Fig. 5g) and clasts with thick bubble walls cut by planar or curved planar surfaces (Fig. 5h).

The mCA beds (Mdφ -1 to 1) are framework-supported and constituted by lithic clasts (up to 70 wt%), subordinate

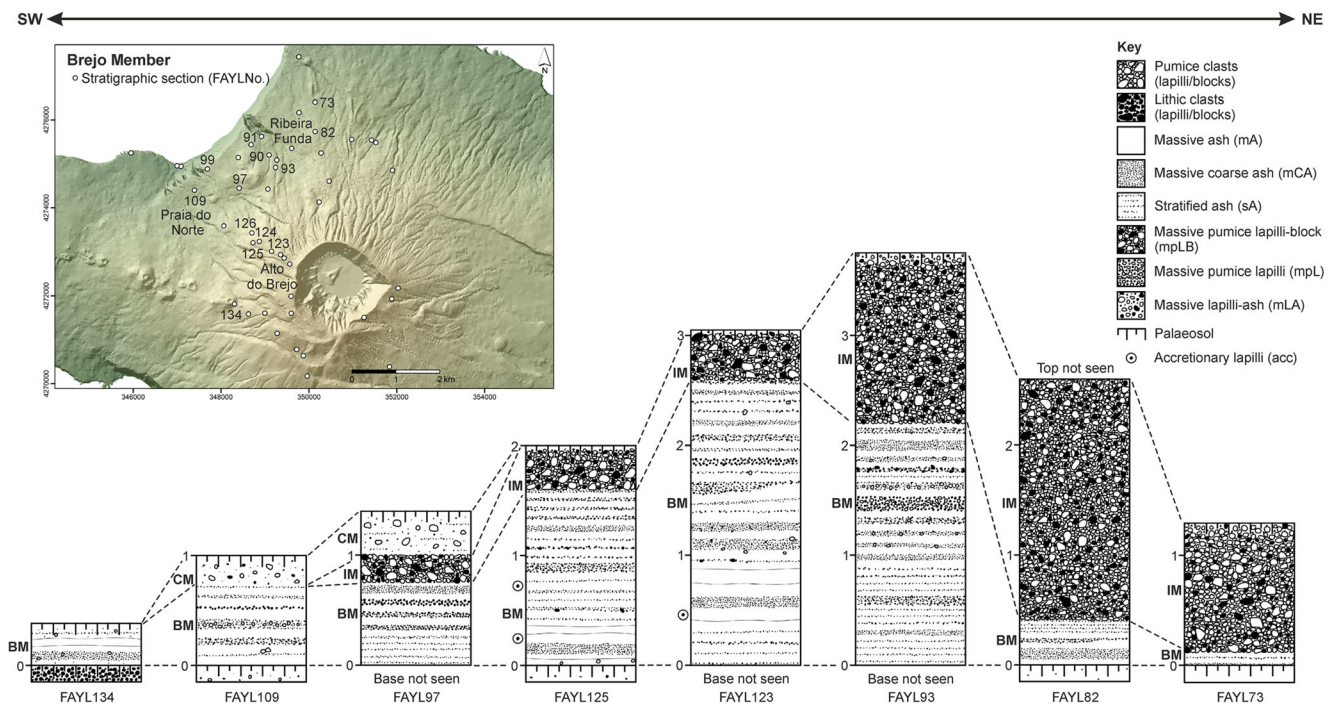


**Fig. 4** Representative stratigraphic sections of Brejo Member showing lateral thickness variation. *BM* Brejo Member, *IM* Inverno Member, *CM* Cedros Member

juvenile clasts and loose crystals. The main lithic clast type is basaltic lava, but hydrothermally altered clasts are also found. Coarser juvenile clasts are pumiceous and predominately angular, although in some beds they show evidence of abrasion.

Several massive pumice lapilli (mpl) beds ( $Md\phi -1$  to  $-1.5$ ) occur intercalated with the ash beds in the upper part of the BM. They are composed of framework-supported pumice and lithic lapilli. Pumice lapilli are angular, generally light-coloured, although banded or dark-grey clasts also occur. Lithic clasts are mainly basaltic lavas, with hydrothermally altered clasts and minor syenite and mafic xenoliths.

The BM beds mantle the topography over several square kilometres, although local, subtle thickness variations in individual beds are present (e.g. FAYL124; Fig. 5c). The upper and lower contacts of beds are commonly sharp. Most beds are internally massive but some show normal or inverse grading. Individual beds are well sorted ( $\sigma\phi$  1–2) to moderately sorted ( $\sigma\phi$  2–3), with unimodal and bimodal particle size distributions (ESM Fig. A.1). Grain size parameters of representative beds are listed on Table 2.

**Distribution** The BM is mainly dispersed across the NW sector of Faial. The isopach map of the ash layers (Fig. 6) indicates a dispersal axis trending N36° W and covering an area of 48 km<sup>2</sup> within the 10-cm isopach. The mA beds are best represented on the western part, towards Praia do Norte, while mCA beds outcrop mostly on the northern part, towards Ribeira Funda.

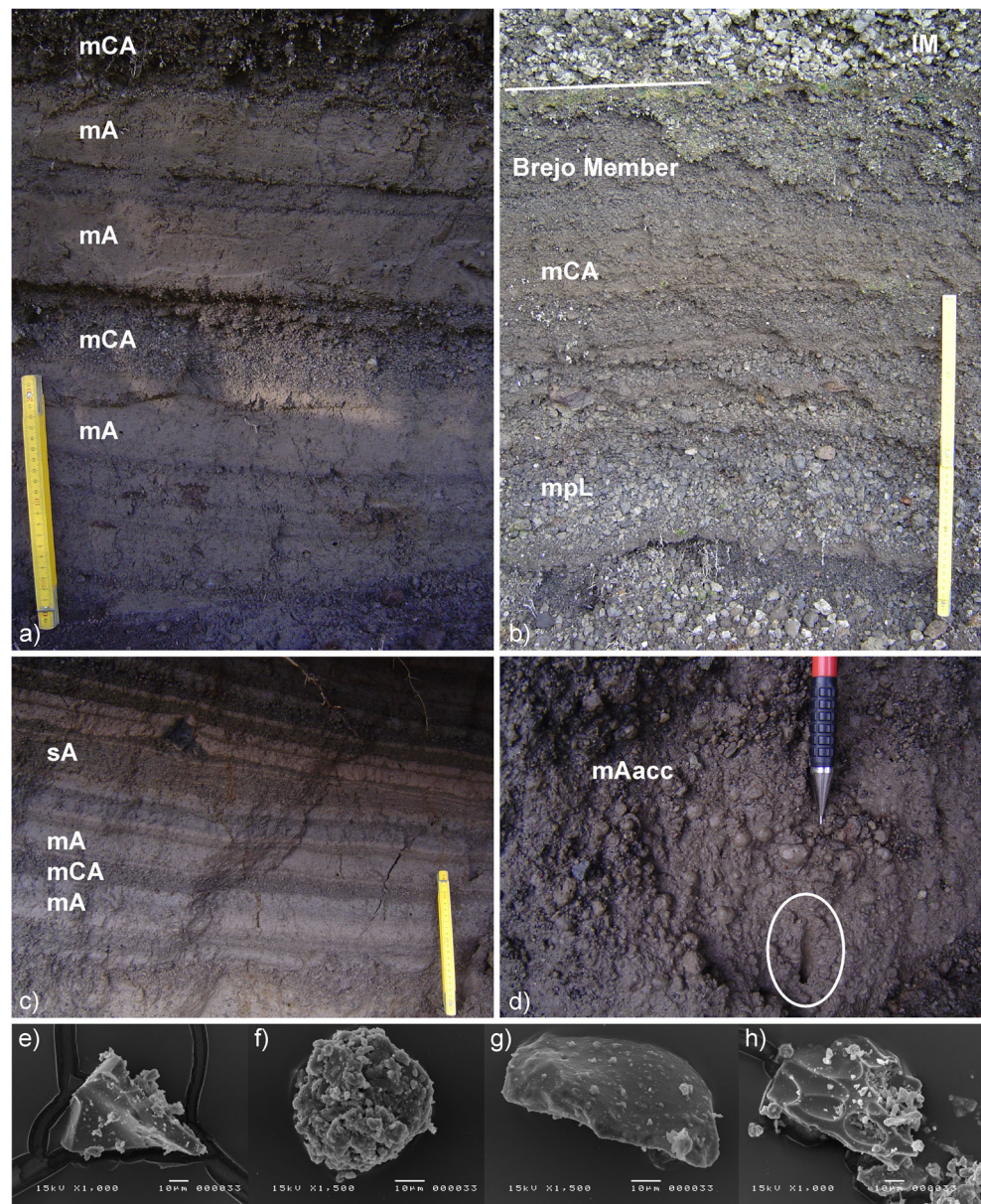
**Interpretation** The //bA layers are consistent with fallout from pulsating eruption columns, associated with the initial phase of the eruption and influenced by wind blowing to the NW. This interpretation is supported by the continuous lateral thickness of the beds (independently of topography) and consistent thinning and fining with distance from the vent. The good sorting in thin beds and the absence of obvious traction structures suggest ash fallout from short-lived columns as the main mode of deposition.

However, some ash beds do show subtle thickness variations, slightly poorer sorting, bimodal particle size distributions and lateral gradations into sA. These beds may have been deposited from short-lived PDCs generated during partial or total column collapses. Although it may be difficult to distinguish the exact depositional mode, it is possible that some beds record gentle ash deposition from fully dilute PDCs, with fallout-dominated flow-boundary zones (Branney and Kokelaar 2002) rather than in a traction regime, or even simultaneous deposition from dilute PDCs and direct ash fallout (Douillet et al. 2013).

The BM ash layers coarsen from base to top. The lower part is primarily composed of mA, sometimes with accretionary lapilli-bearing beds, while the upper part comprises mCA and occasional mpl beds. This suggests that magma fragmentation efficiency decreased with time during the initial phase of the eruption.

The presence of very fine-grained mA beds ( $Md\phi$  4–5) and high lithic contents is consistent with phreatomagmatic activity (Wohletz 1983; Barberi et al. 1989; Dellino and La Volpe

**Fig. 5** Deposits from Brejo Member at different stratigraphic sections (see Fig. 4 for location and Table 1 for lithofacies key). **a** Sequence of massive fine-grained ash beds and subordinate coarse-grained ash beds (FAYL126; scale is 20 cm). **b** Sequence of massive coarse-grained ash beds and a massive pumice lapilli bed (FAYL90; scale is 40 cm), *IM* Inverno Member. **c** Stratified ash bed with local thickness variation in a sequence of parallel-bedded ash beds (FAYL124; scale is 20 cm). **d** Accretionary lapilli (*ash pellets*) and branch mould, within the circle, in a fine-grained ash bed (FAYL123, pen for scale). SEM images **e** to **h** show different morphologies of juvenile ash particles. **e** Dense blocky clast (FAYS103-1). **f** Subrounded clast with moss-like morphology (FAYS103-1). **g** Fused-shaped poorly vesicular clast (FAYS123-1). **h** Vesicular clast with thick walls cut by planar surfaces (FAYS123-3)



1995). Also, the various morphologies of the juvenile ash particles (Fig. 5e–h) reflect varying degrees of water-magma interaction (Wohletz 1983; Pardo et al. 2009). Furthermore, the presence of mAacc suggests input of external water. Moist ash deposits are associated with phreatomagmatic eruptions (e.g. De Rita et al. 2002) but may also result from magmatic eruptions in high humidity atmospheric conditions (e.g. Cole et al. 2002).

Together this evidence supports an early phreatomagmatic phase. Phreatomagmatism is a common feature of the Upper Group of Cedros Volcanic Complex and several other deposits show evidence of water-magma interaction (C2, C7, C9 and C12; Pacheco 2001), suggesting that Caldeira Volcano had crater ponds or sustained aquifers over the past 16 kyr.

At later stages, magmatic fragmentation became dominant as indicated by the presence of coarser vesicular clasts, particularly in mpL beds of the upper part of BM.

### Inverno Member

The IM is a coarse-grained pumice deposit that is clearly distinct from the underlying BM. It is best represented near Alto do Inverno (type location FAYL82; Fig. 7), where it is >2 m thick and is composed of two massive pumice lapilli-block (mpLB) beds, A and B, separated by an inconspicuous massive coarse-grained ash (mCA) layer (Fig. 8a).

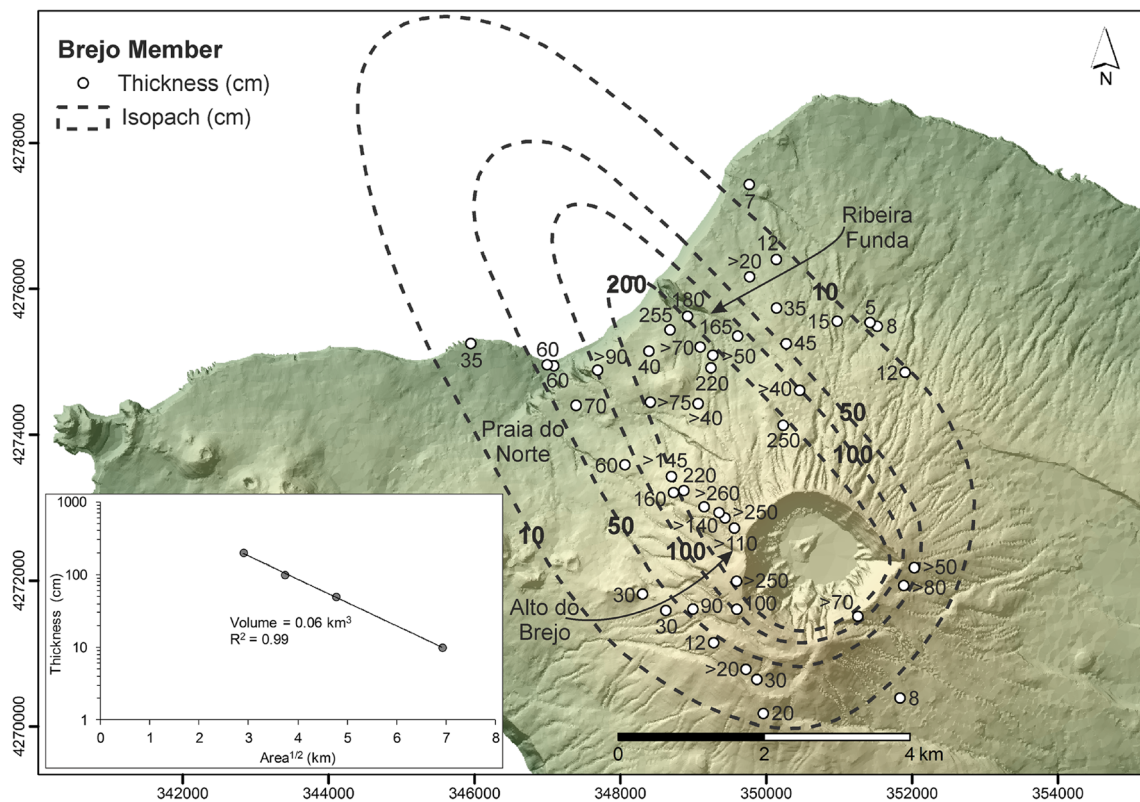


**Fig. 6** Isopach map of the Brejo Member ash layers; UTM coordinates, zone 26S. Inset shows log of thickness vs. square root of area diagram

**Lithofacies** The mpLB consist of framework-supported coarse-grained ( $Md\phi \sim 4$ ) pumice and lithic lapilli (Fig. 8b) with abundant blocks (pumice and lithic clasts up to 45 and 25 cm, respectively). Pumice clasts (up to 70 wt%) are angular and frequently show impact fractures (Fig. 8c). They are typically banded of light colour (beige) and dark-grey, but uniform coloured clasts are common. Light-coloured/banded clasts are more vesicular than dark-grey clasts (Fig. 8d). Lithic clasts are subordinate and are mostly basaltic lavas, but frequent hydrothermally altered clasts and syenite xenoliths are found. Occasionally, mafic cumulate xenoliths are also present.

The mpLB is well sorted ( $\sigma\phi$  1–2; ESM Fig. A.2) without obvious internal structures, although in some localities a tendency towards inverse-normal grading is observed (e.g. FAYL94). It mantles the topography and ranges in thickness from 0.15 to >2.5 m. The upper and lower contacts are well defined with sharp boundaries. Occasionally, the top of the upper bed B is marked by an erosion surface caused by later PDCs.

The mCA layer, found between the pumice beds, is composed of juvenile ash with occasional fine-grained pumice and lithic lapilli. It is typically thin, <10 cm, and sometimes absent from the pumice deposit. The top and base show diffuse boundaries.

**Distribution** The IM has a restricted distribution in the northern sector of the island. The isopachs of the pumice deposit are

narrow, with a single dispersal axis trending N12° W; the 25-cm isopach covers an area of 26 km<sup>2</sup> (Fig. 9). As the ash layer is not ubiquitous throughout the outcrops, individual isopach maps of beds A and B were not produced.

**Interpretation** The IM records the second phase of the eruption. The mpLB lithofacies is interpreted as a pumice fall deposit deposited from an eruption column influenced by strong wind blowing to the NNW. This interpretation is based on characteristics of the deposit such as consistent thinning and fining with distance from the vent, framework-supported nature and good sorting. Also the occurrence of angular pumice with impact fractures is consistent with fallout. The coarseness of the deposit reveals that transport by ballistic trajectory also played an important role during deposition.

The presence of two pumice beds indicates unsteadiness of the eruption column. However, as the mCA layer is not ubiquitous, it suggests that the unsteadiness may represent only a brief oscillation in the column, rather than a complete pause.

The inconspicuous mCA is interpreted as an ash fall layer based on its relatively continuous thickness and absence of internal structures. This bed records the deposition of residual ash suspended in the atmosphere between oscillations of the eruption column (e.g. Brown and Branney 2004).

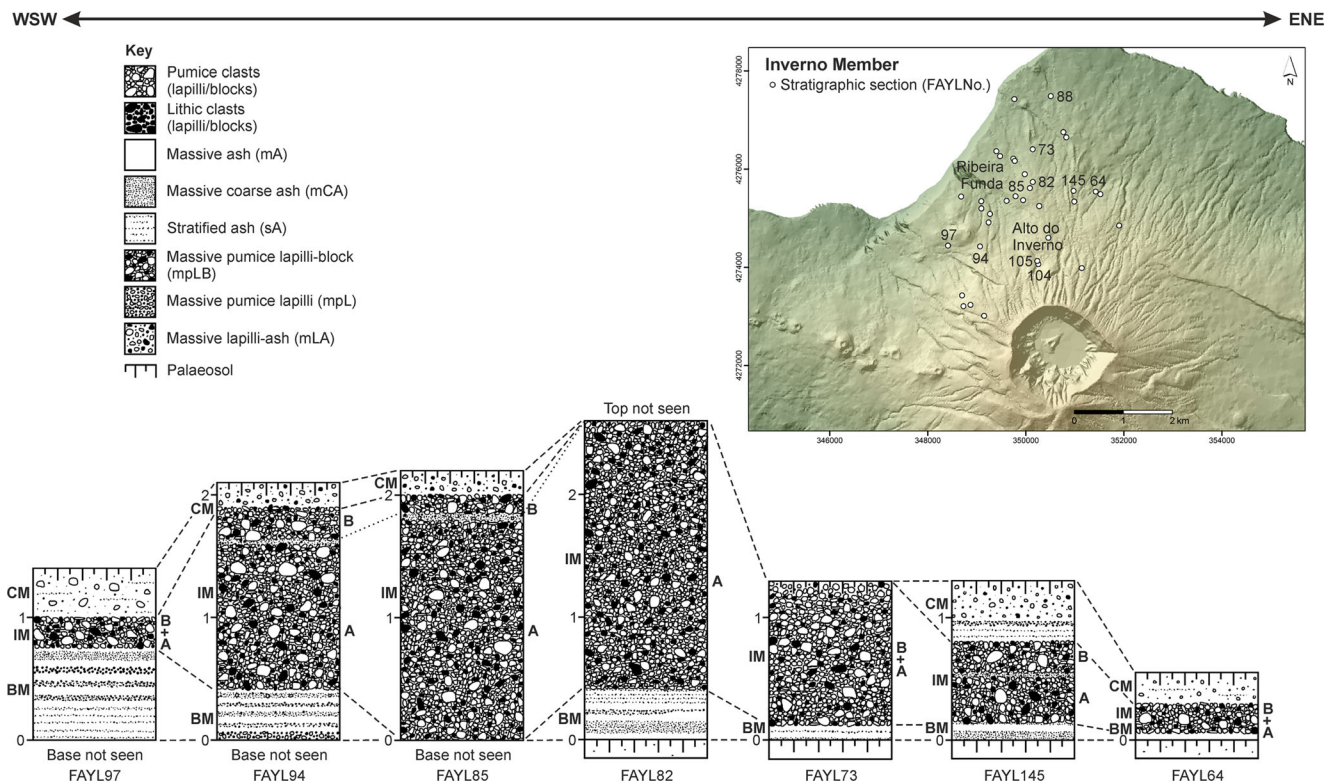


**Fig. 7** Representative stratigraphic sections of Inverno Member showing lateral thickness variation. *BM* Brejo Member, *IM* Inverno Member, *A* Bed A, *B* Bed B, *CM* Cedros Member

### Cedros Member

The CM is an ignimbrite sheet characterised by several lithofacies, ranging from various types of lapilli-ash to lithic breccia (IBr). It is named after the town of Cedros (type location FAYL46; Fig. 10), where thick lapilli-ash deposits (>4 m) are well exposed. CM comprises different intergradational lithofacies (Fig. 11): massive lapilli-ash (mLA), diffuse-bedded lapilli-ash (dbLA), diffuse-stratified lapilli-ash (dsLA), stratified lapilli-ash (sLA), massive lithic breccia (mlBr) and diffuse-bedded lithic breccia (dblBr).

**Lithofacies** The lapilli-ash deposits exhibit closely spaced lateral and vertical variations. They are topographically controlled with large thickness variations over a few metres, sometimes reaching >7 m in thickness.

The mLA is the most commonly seen lithofacies of CM (Fig. 11a). It is matrix-supported and poorly sorted ( $\sigma\phi$  2–4), with polymodal particle size distributions and variable proportions of pumice and lithic clasts (ESM Fig. A.3) in a grey ash matrix with abundant loose crystals. Grain size parameters of representative CM samples are listed in Table 2.

Pumice clasts are rounded to subrounded, ranging from banded to light-coloured and dark-grey. Lighter coloured clasts are more vesicular than the darker coloured ones. Lithic

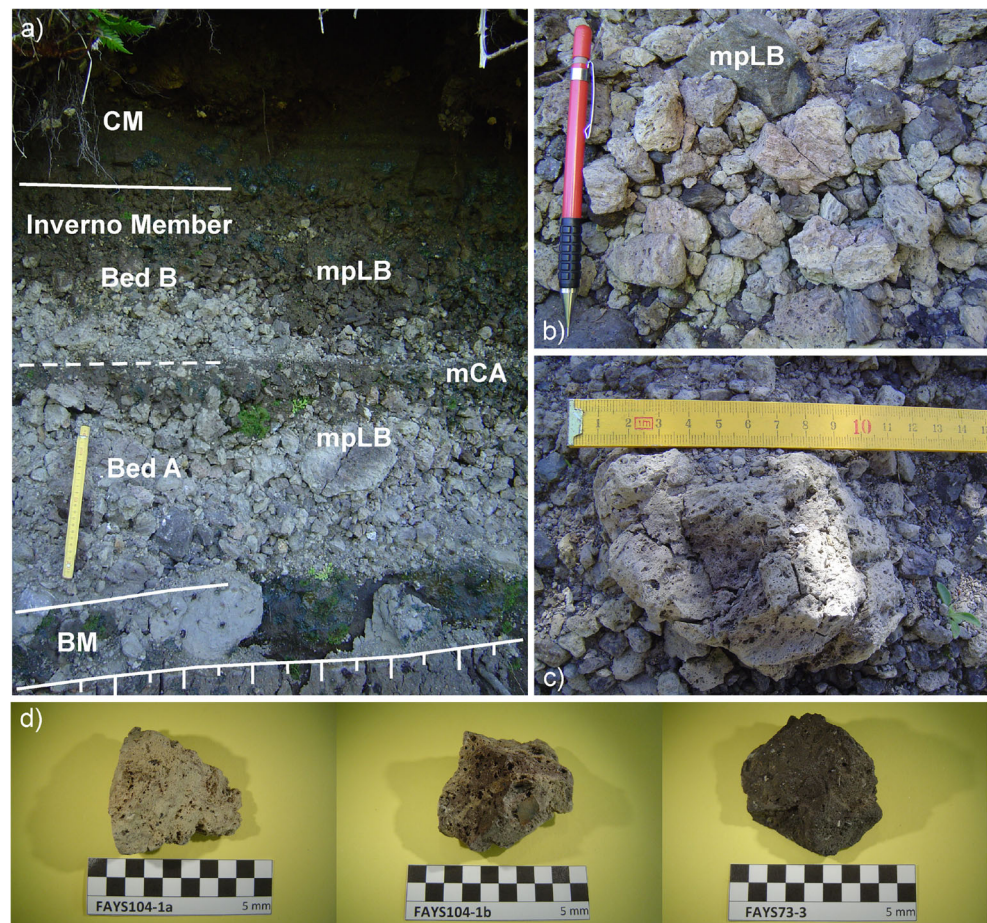
clasts (frequently up to 50 wt%) are angular to subrounded and are mostly basaltic lavas, hydrothermally altered clasts, syenite xenoliths and few mafic cumulate xenoliths. Lapilli-size clasts are dominant, although coarser clasts are common at certain locations (e.g. Fajã beach and Alto do Inverno). Pumice and lithic blocks can reach up to 20 and 185 cm, respectively. Abundant carbonised wood fragments and standing tree trunks are common in this lithofacies.

The mLA deposits are generally structureless. However, lithic-rich or pumice-rich lenses of rounded to subrounded framework-supported lapilli and blocks (pLBlens, ILBlens) and fines-poor lithic-rich pipes (lpip) are present.

The dbLA lithofacies is poorly sorted ( $\sigma\phi$  2–4) and composed of the same components as mLA. The internal structure is defined by decimetre-thick parallel to subparallel beds (Fig. 11b). Individual beds, marked by pumice-rich or lithic-rich horizons, are massive or show simple grading patterns. Beds are laterally continuous for a few metres, although gradual thickening or thinning also occurs. Tops and bases of individual beds show diffuse boundaries. Thicker beds occasionally exhibit pLBlens or ILBlens.

The dsLA is also poorly sorted ( $\sigma\phi$  2–3) but finer grained than dbLA (pumice clasts <7 cm and lithic clasts <5 cm), with the same component characteristics as in the mLA. The internal structure is defined by very thin layers (typically <1 cm), with parallel to subparallel stratification (Fig. 11c). Individual

**Fig. 8** Features of Inverno Member at stratigraphic section FAYL145 (see Fig. 7 for location and Table 1 for lithofacies key). **a** Beds A and B (scale is 20 cm. *BM* Brejo Member, *CM* Cedros Member). **b** Framework-supported coarse-grained pumice and lithic lapilli. **c** Pumice block with impact fractures. **d** Light-coloured, banded and dark-grey pumice clasts



layers are massive, but also show normal or inverse grading. The layering is diffuse and marked by alternating ash-rich and lapilli-rich layers. Some layers have sharp boundaries that define sLA lithofacies. Lateral thickness variations of individual layers are common.

The lBr is matrix-supported, less frequently framework-supported and poorly sorted and reaches >3 m in thickness (Fig. 11d). Lithic clasts are angular and very poorly sorted (blocks up to 130 cm). They comprise basaltic lavas and common hydrothermally altered clasts and syenite xenoliths. Occasionally, mafic cumulate xenoliths are present. Pumice clasts are subordinate, poorly sorted (generally <20 cm) and variably vesicular, as banded, light-coloured or dark-grey clasts. Most are angular, with coarser clasts frequently showing impact fractures. Sporadic carbonised wood fragments are found. The pumiceous lapilli-ash matrix is poorly sorted (e.g.  $\phi$  2.58; FAYS30-1) and contains abundant loose crystals.

Typically, the lBr deposits are massive (mlBr), but a few outcrops show normal grading of lithic clasts (e.g. FAYL103) and diffuse-bedding (dblBr; FAYL30). Stratigraphically, they tend to occur above the lapilli-ash lithofacies. The lower part is coarser and the boundaries may be diffuse or sharp, occasionally showing impact sags produced by large lithic blocks

sinking into the underlying ash layers of BM. The upper part is finer grained, pumice-rich and marked by a palaeosol.

The base of CM commonly rests on top of IM or older deposits, and less frequently, it overlies BM. The top of CM is marked by a palaeosol or more rarely an erosion surface.

**Distribution** The CM is widely found on the central part of Faial, spreading to the north and east flanks of Caldeira Volcano (Fig. 12), and covers a minimum inland area of 39 km<sup>2</sup>. Two main flow paths are identified: the north path is widespread along the slopes of the volcano to the coastline; while the Pedro Miguel path is confined by the fault scarps of the graben. The thickest deposits (>7 m) occur at proximal locations on the northern sector and in patches at medial and distal areas (e.g. Fajã beach, Cascalho, Canada Larga, Cancelas; Fig. 12).

The lapilli-ash lithofacies are best represented between >500 m from the summit and the coastline on the west and north sectors of Faial (at distances of 3–5 km) and along Pedro Miguel stream-valley (~9 km away). The mLA, dbLA and lithic-rich lithofacies commonly occur in palaeovalleys or flatter areas, where the deposits are thicker, while dsLA and sLA

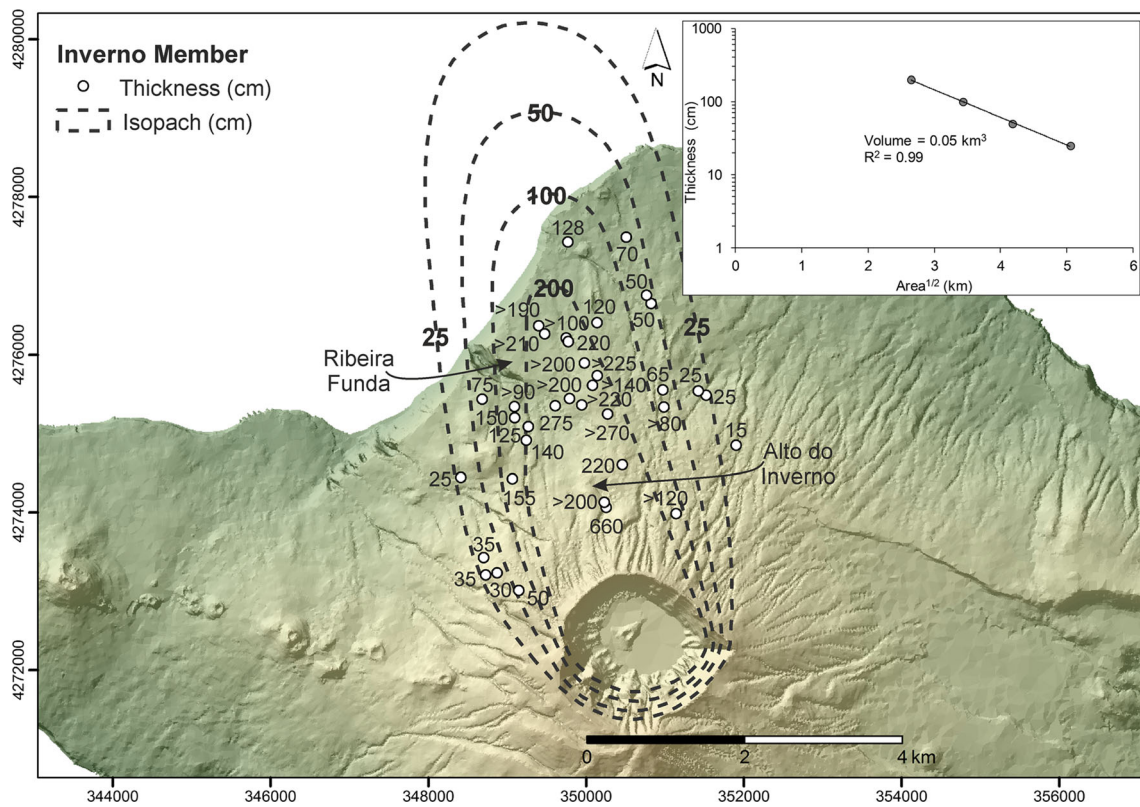


**Fig. 9** Isopach map of the Inverno Member coarse pumice fall; UTM coordinates, zone 26S. *Inset* shows log of thickness vs. square root of area diagram

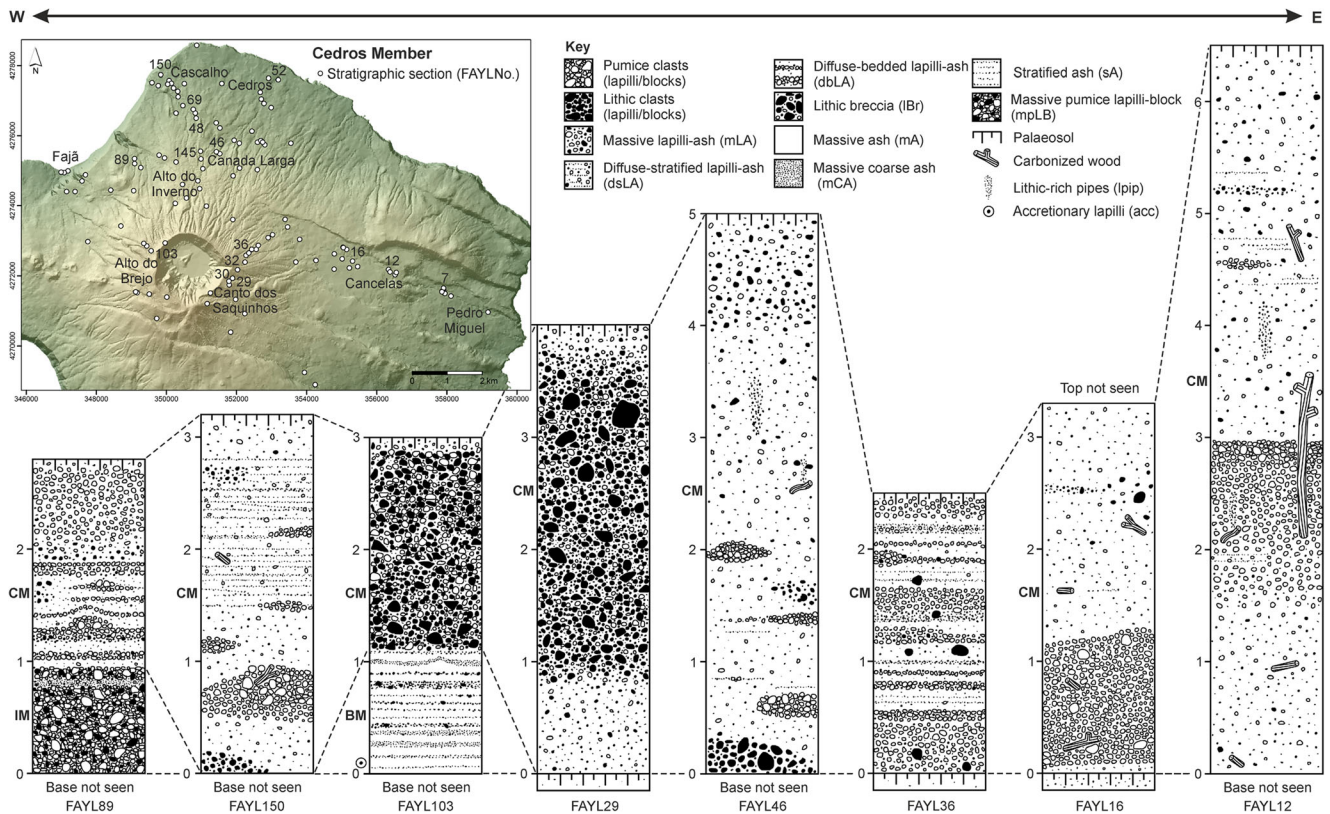
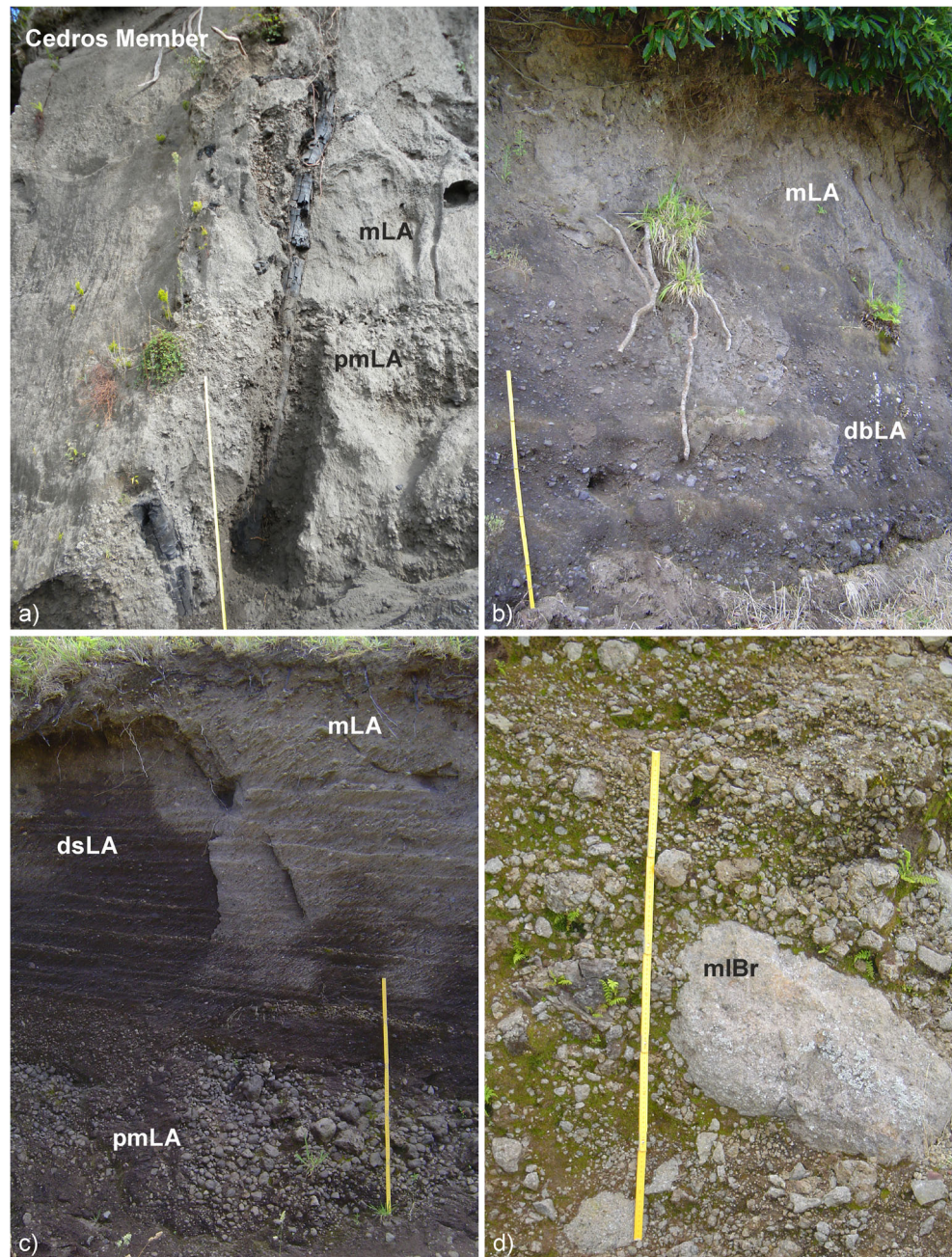


**Fig. 10** Representative stratigraphic sections of Cedros Member showing thickness and lithofacies variations. *BM* Brejo Member, *IM* Inverno Member, *CM* Cedros Member

**Fig. 11** Deposits from Cedros Member at different stratigraphic sections (see Fig. 10 for location and Table 1 for lithofacies key; scale is 1 m). **a** Massive lapilli-ash with pumice-rich horizon and standing charred tree trunk (FAYL12). **b** Lithic-rich diffuse-bedded lapilli-ash grading into massive lapilli-ash (FAYL69). **c** Pumice-rich massive lapilli-ash grading to diffuse-stratified lapilli-ash and to massive lapilli-ash (FAYL150). **d** Massive lithic breccia (FAYL32)



tend to occur in the higher ground or where the deposits are thinner. The lBr are dominant at proximal locations ( $\leq 500$  m from the summit) mainly along the northern part.

**Interpretation** The various lapilli-ash deposits are interpreted as different lithofacies of an ignimbrite deposited from high particle concentration PDCs during the final phase of the eruption. This interpretation is based on the matrix-supported nature of the deposits, poor sorting, polymodal particle size distributions, variable internal structures and abundance of charred tree trunks. Also, the closely spaced

intergradations of lithofacies and significant lateral thickness variations indicate a flow origin for these deposits.

The mLA deposits were formed by the rapid progressive aggradation of pyroclasts from high particle concentration granular fluid-based PDCs (e.g. Branney and Kokelaar 2002; Brown et al. 2007; Sulpizio et al. 2007; Sulpizio and Dellino 2008). Their poor sorting and massive nature suggests deposition from PDCs with fluid escape-dominated flow-boundary zones (Branney and Kokelaar 2002), where pyroclasts are supported by the upward escape of interstitial fluid as consequence of deposition (i.e. hindered settling). The

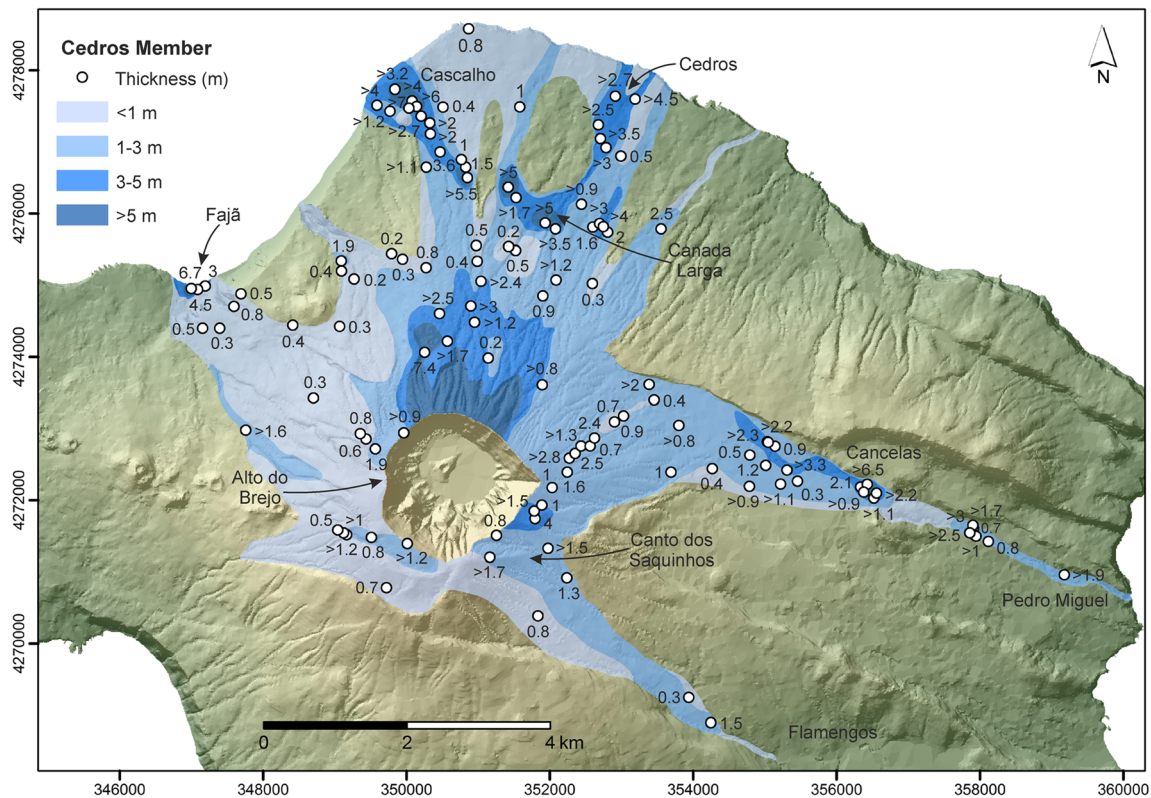


**Fig. 12** Distribution map of the Cedros Member PDC deposits; UTM coordinates, zone 26S

lack of internal structures indicates that steady conditions were dominant during sustained deposition from PDCs (Branney and Kokelaar 2002; Sulpizio and Dellino 2008).

The dbLA records PDC unsteadiness during deposition, with flow-boundary zones that were gradational between fluid escape- to granular flow-dominated, rather than deposition from separate currents. The dsLA records the development of flow-boundary zones between fluid escape- and granular flow-dominated and short periods of traction-dominated regimes which deposited sLA (Branney and Kokelaar 2002).

The lateral intergradations of thick mLA and dbLA in palaeovalleys with thinner dsLA and sLA in topographic highs have been recognised in ignimbrites elsewhere (e.g. Wilson 1985; Scott et al. 1996; Giordano et al. 2002; Brown and Branney 2004, 2013) and correspond to valley-fill to veneer lithofacies transitions.

The distribution and lithofacies associations suggest that the CM ignimbrite was deposited from sustained quasi-steady PDCs generated by prolonged pyroclastic fountaining and that were strongly controlled by topography. These characteristics are indicative of low mobility, high particle concentration currents, very sensitive to subtle slope changes and unable to overcome obstacles (e.g. Branney and Kokelaar 2002; Giordano et al. 2002).

The lBr are consistent with proximal PDC lithofacies on the basis of their poor sorting, chaotic nature and

pumiceous matrix. The down-slope gradation into mLA or dbLA indicates that they are the proximal equivalent of an ignimbrite. The lBr also includes an important fall-out component revealed by the large lithic blocks and coarse angular pumice clasts with impact fractures. The presence of lithic block impact sags on the underlying BM indicates ballistic transport.

Nevertheless, the abundance and size of the lithic clasts (basaltic lavas, hydrothermally altered clasts, syenite and mafic cumulate xenoliths, in decreasing order of abundance) indicate that conduit wall erosion and most summit collapse occurred during this phase of the eruption.

## Physical parameters of the eruption

### Volume estimates

On a small island such as Faial (~170 km<sup>2</sup>), it should be noted that the values presented are minimal values because of the unknown portion of material deposited offshore, as commonly seen in small islands elsewhere (Walker 1981). The fallout volumes of BM and IM were calculated following Pyle (1989) modified by Fierstein and Nathenson (1992). In both cases, isopachs are regularly spaced (Figs. 6 and 9),

suggesting that thickness decreases at an exponential rate with distance from the vent. The log of thickness vs. square root of area diagrams (insets on Figs. 6 and 9) show that data are best fitted by a single line segment. Thus, the calculated volumes correspond only to proximal bulk volumes. To overcome this issue, the empirical method of Sulpizio (2005) was combined with Fierstein and Nathenson (1992) to obtain the total bulk volumes from the estimation of distal volumes deposited at sea (Table 3).

The BM has a proximal bulk volume of  $0.06 \text{ km}^3$  and an estimated total bulk volume of  $0.08 \text{ km}^3$ . The latter corresponds to a deposit mass of  $6.9 \times 10^{10}$  to  $9.2 \times 10^{10} \text{ kg}$ , based on ash densities of  $900\text{--}1200 \text{ kg/m}^3$  (obtained by weighing compacted representative samples in  $500 \text{ cm}^3$  beakers). A dense rock equivalent (DRE) volume between  $0.03$  and  $0.04 \text{ km}^3$  was calculated considering the deposit mass range and a trachytic magma density of  $2400 \text{ kg/m}^3$  (obtained from whole-rock composition and geothermometry; see next section).

The IM yields a proximal bulk volume of  $0.05 \text{ km}^3$  and an estimated total bulk volume of  $0.07 \text{ km}^3$ . This is significantly smaller than proposed by Pacheco (2001), who estimated a volume of  $0.11 \text{ km}^3$  for the same deposit, based on a 6-m isopach drawn around a single point. The present total bulk volume can be converted to a DRE volume of  $0.01 \text{ km}^3$ , using a deposit mass of  $3.3 \times 10^{10} \text{ kg}$ , obtained from an average pumice fall deposit density of  $500 \text{ kg/m}^3$  and the trachytic magma density.

Nevertheless, the fallout volumes obtained here must be considered minima, because of the lack of distal outcrops. They may be underestimated by  $>50 \%$  when compared with other similar fallout deposits with better distal constraints (e.g. Sahetapy-Engel et al. 2014; ESM Fig. A.4).

The CM bulk volume was calculated by multiplying the area of each isopach polygon by its representative thickness

(Fig. 12). The minimum bulk volume on land is  $0.07 \text{ km}^3$ , which is in good agreement with  $0.06 \text{ km}^3$  estimated by Caniaux (2012). Both these values do not account for the volume of material deposited at sea by PDCs. The bulk volume corresponds to a deposit mass of  $7.8 \times 10^{10} \text{ kg}$ , using an average density of  $1200 \text{ kg/m}^3$  for the PDC deposits. A minimum DRE volume estimate of  $0.03 \text{ km}^3$  was obtained using the mass value and the trachytic magma density.

In summary, the bulk volume of the C11 eruption is conservatively estimated at  $>0.22 \text{ km}^3$ . This corresponds at least to a volcanic explosivity index (VEI) 4 event (Newhall and Self 1982) with a magnitude of 4.2 to  $>4.3$  (Pyle 2000). The minimum DRE volume is thus estimated to have been between  $0.07$  and  $>0.08 \text{ km}^3$ . It is reasonable to assume that  $>0.1 \text{ km}^3$  DRE volume of magma was involved in the eruption, considering the unknown portion of material deposited into the sea.

The total volume of the C11 eruption is unknown. However, if we assume that the minimum bulk volume estimate (at least  $0.22 \text{ km}^3$ ) is about one third of the total, as previously considered for other eruptions on Azores (e.g. Fogo A: Walker and Croasdale 1971 and Lajes-Angra Ignimbrite: Self 1976), then the total bulk volume of the eruption is  $>0.66 \text{ km}^3$  (i.e.  $>0.3 \text{ km}^3$  DRE).

Pacheco (2001) suggested a total bulk volume of  $>0.7 \text{ km}^3$  for this eruption, roughly corresponding to the volume of the summit caldera and in close agreement with the present estimate. Following this approach and assuming a volume of  $0.68 \text{ km}^3$  (calculated from an inverted truncated cone with top and basal diameters of 2 and 1 km, respectively, and average depth of 370 m), then  $\sim 67 \%$  of the material is missing and may be deposited offshore. A summary of the physical parameters of the C11 eruption and its members is presented on Table 3.

**Table 3** Summary of the physical parameters of the deposits from the C11 eruption

Physical parameter	Brejo Member	Inverno Member	Cedros Member	Total C11
Proximal bulk volume ( $\text{km}^3$ ) <sup>a</sup>	0.06	0.05	0.07	0.18
Total bulk volume ( $\text{km}^3$ ) <sup>b</sup>	0.08	0.07	—	$>0.22$
VEI <sup>c</sup>	3	3	3?	4
Deposit mass ( $\times 10^{10} \text{ kg}$ ) <sup>d</sup>	6.9–9.2	3.3	$>7.8$	$18.0\text{--}>20.3$
Magnitude <sup>e</sup>	3.8–4.0	3.5	$>3.9$	$4.2\text{--}>4.3$
DRE volume ( $\text{km}^3$ ) <sup>f</sup>	0.03–0.04	0.01	$>0.03$	$0.07\text{--}>0.08$

<sup>a</sup> Fallout after Pyle (1989) modified by Fierstein and Nathenson (1992). PDC deposits from the sum of polygon areas multiplied by representative thickness

<sup>b</sup> Fallout after Sulpizio (2005) combined with Fierstein and Nathenson (1992). Not applicable for PDC deposits

<sup>c</sup> After Newhall and Self (1982)

<sup>d</sup> Based on an average compacted deposit density of  $900\text{--}1200$ ,  $500$  and  $1200 \text{ kg/m}^3$  for ash, pumice fall and ignimbrite, respectively

<sup>e</sup> After Pyle (2000)

<sup>f</sup> Based on a trachytic magma density of  $2400 \text{ kg/m}^3$  and deposit mass values

### Column height and mass eruption rate

Eruption column height was calculated for the second phase (IM) following the method of Carey and Sparks (1986), but not for initial phase due to the pulsating nature of the columns.

The IM isopleth maps (Fig. 13a, b) are oriented towards NNW closely resembling the isopach map (Fig. 9). The maximum downwind and crosswind ranges obtained from the lithic clast isopleths (Fig. 13a) were plotted on the Carey and

Sparks (1986) diagram for 6.4 cm diameter clasts (Fig. 13c), giving a maximum column height of ~14 km and wind speeds of 25 m/s. Estimates made using coarse lithic clasts tend to give lower column heights than those with fine-grained clasts.

The mass eruption rate (MER) was calculated using the method of Wilson and Walker (1987), yielding  $1.2 \times 10^7$  kg/s, which corresponds to an intensity of 10 (Pyle 2000). This MER must be a peak value because the column showed slight oscillations, recorded by the ash layer in the pumice fall

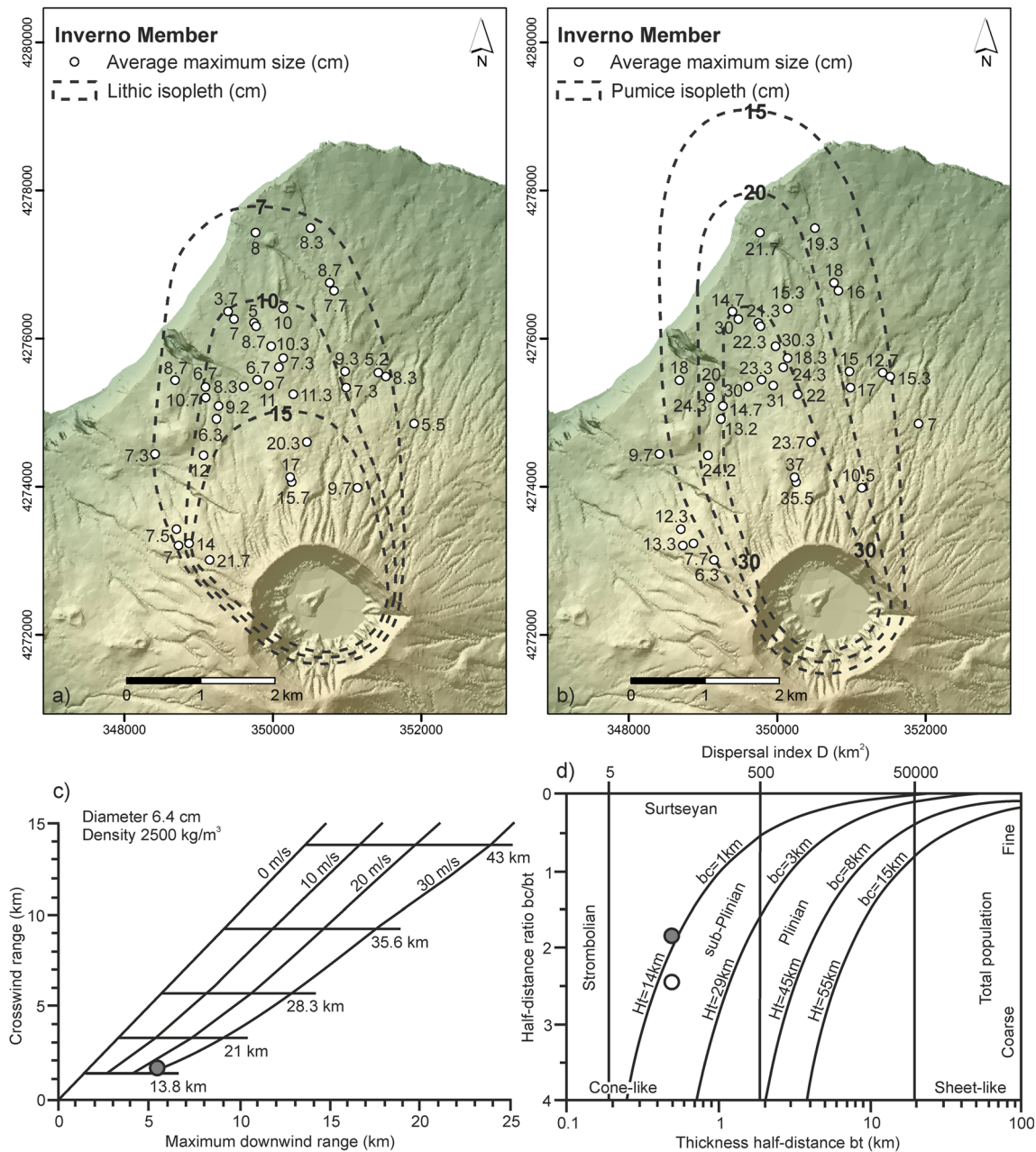


**Fig. 13** Isopleth maps of the Inverno Member. **a** Lithic clast isopleths. **b** Pumice clast isopleths; UTM coordinates, zone 26S. **c** Crosswind range vs. downwind range diagram for 6.4 cm clast diameter with 2500 kg/m<sup>3</sup> of density (Carey and Sparks 1986). **d** Half-distance ratio (bc/bt) vs.

thickness half-distance diagram (bt), where bc is the clast half-distance and Ht is the total column height (Pyle 1989). Grey marker—lithic clasts; white marker—pumice clasts

deposit. An approximate duration of ~45 min was obtained, by dividing the deposit mass by the peak MER.

The eruptive style was classified following the Pyle (1989; Fig. 13d) diagram, using the half-distance ratio (bc/bt) vs. thickness half-distance (bt), where bc is the clast half-distance. From the isopach (Fig. 9) and isopleth maps (Fig. 13a, b), IM pumice fall has a bt of 0.4, while the bc values for lithic and pumice clasts are 0.8 and 1.1, respectively. These plot in the transition from Strombolian to sub-Plinian fields in the case of the lithic clasts and in the sub-Plinian field for the pumice clasts, suggesting that this phase had an overall sub-Plinian style. The large bc/bt values (1.8 for lithics and 2.6 for pumices) are indicative of small dispersal, typical of coarse-grained fall deposits. The column height obtained from the lithic clasts on the diagram of Pyle (1989) is ~14 km, which is in good agreement with that calculated using the method of Carey and Sparks (1986).

## Petrography and geochemistry

### Petrographic aspects and mineral chemistry

The juvenile products of C11 comprise light-coloured (beige), dark-grey and banded pumice clasts. A brief macroscopic description and correspondence with the members are reported in Table 4.

Light-coloured clasts (~42 vol% vesicularity) have a low phenocryst content (1.5–3 vol%) and a glassy hypocrySTALLINE groundmass. The vesicles are subcircular to slightly elongated and separated by thin walls (Fig. 14a). By contrast, dark-grey clasts (~19 vol% vesicularity) have higher phenocryst contents (8 vol%) in a glassy groundmass with a higher microlite content. These often show seriate texture and smaller irregularly shaped to subcircular vesicles with thicker walls (Fig. 14b). Banded pumice clasts show features common to both types of clasts, at a meso- and micro-scale.

The juvenile products share the same mineral assemblage: plagioclase, alkali feldspar, olivine, amphibole, biotite, clinopyroxene, Fe-Ti oxides and occasional apatite. There

are no significant differences in the mineral compositions among the different juvenile products (ESM Table A.1).

Plagioclase ( $An_{16-79}$ ,  $Ab_{21-76}$ ,  $Or_{1-9}$ ) is the most abundant mineral phase ( $\leq 5$  vol% phenocrysts) and occurs as euhedral and subhedral phenocrysts to microlites. Phenocrysts ( $\leq 2.5$  mm) are frequently fractured and occasionally show features of disequilibrium with the host rock (e.g. partially resorbed rims and sieve textures). Alkali feldspar ( $An_{1-15}$ ,  $Ab_{60-74}$ ,  $Or_{10-38}$ ) is also present as euhedral and subhedral phenocrysts ( $\leq 1.6$  vol%) to microlites. Some anorthoclase phenocrysts ( $\leq 1.5$  mm) are fractured and partially resorbed with reaction rims composed by Fe-Ti oxides and amphibole.

Olivine is less common ( $\leq 1$  vol%) and occurs as phenocrysts ( $\leq 0.4$  mm) and microphenocrysts which frequently show partially resorbed rims and rounded edges, that sometimes host Fe-Ti oxides. Its chemical composition ( $Fe_{67-79}$ ) is in disequilibrium with the host rock, indicating a xenocrystic origin.

Amphibole (kaersutite and Mg-hastingsite) is found as euhedral to anhedral phenocrysts ( $\leq 0.4$  vol%) and rarely as microlites. Phenocrysts ( $\leq 0.5$  mm) occasionally show signs of disequilibrium (i.e. embayments and anhedral forms). Clinopyroxene (diopside and augite;  $Wo_{29-47}$ ,  $En_{30-42}$ ,  $Fs_{12-36}$ ) is present as euhedral and subhedral phenocrysts ( $\leq 0.3$  vol%) to microphenocrysts; aegirine-augite crystals are rare. Biotite is found as euhedral and subhedral phenocrysts ( $\leq 0.4$  vol%) and rarely as microlites and frequently shows disequilibrium features.

Fe-Ti oxides occur as euhedral to anhedral phenocrysts ( $\leq 0.4$  vol%) to microlites. Microphenocrysts of Fe-Ti oxides are also found as inclusion in other mineral phases. Magnetite (46–62 mol% Usp) strongly prevails over ilmenite (85–90 mol% Ilm). Apatite is rare and found only as microphenocrysts.

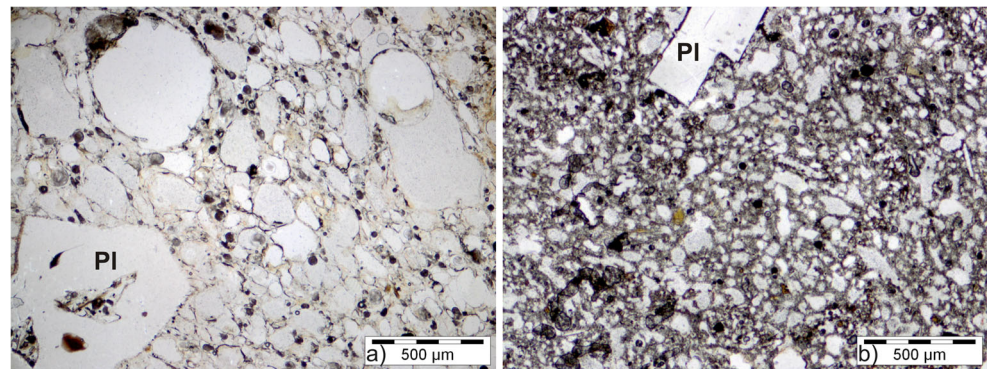
### Whole-rock and glass geochemistry

Whole-rock and groundmass glass compositions of C11 juvenile products are summarised in Table 5 (full whole-rock analyses in ESM Table A.2). The pumices are classified as

**Table 4** Brief macroscopic description of the samples and correspondence with the C11 members (see Figs. 4, 7 and 10 for location and Table 1 for lithofacies key)

Member	Sample	Lithofacies	Main macroscopic features
Brejo	FAYS91-1	mpL	Angular, vesicular and light-coloured
Brejo	FAYS99-1	mpL	Angular, vesicular and light-coloured
Inverno	FAYS73-3	mpLB	Angular, poorly vesicular and dark-grey
Inverno	FAYS104-1a	mpLB	Angular, vesicular and light-coloured
Inverno	FAYS104-1b	mpLB	Angular, vesicular and banded
Inverno	FAYS104-1c	mpLB	Angular, vesicular and dark-grey
Cedros	FAYS7-1a	mLA	Rounded, vesicular and banded
Cedros	FAYS7-1b	mLA	Subrounded, vesicular and banded

**Fig. 14** Microphotographs of C11 juvenile products, in plane-polarised light (*Pl* plagioclase phenocryst). **a** Light-coloured pumice with large vesicles and subhedral plagioclase phenocryst. **b** Dark-grey pumice with small irregularly shaped vesicles and euhedral plagioclase phenocryst



trachyte with 59 wt%  $\text{SiO}_2$  and 10 wt% of  $\text{Na}_2\text{O} + \text{K}_2\text{O}$ . The groundmass glass composition ranges from 60 to 67 wt%  $\text{SiO}_2$ , also lying in the trachyte field, with a few samples on the benmoreite-trachyte boundary (Fig. 15).

The analysis of whole-rock diagrams of major elements vs.  $\text{SiO}_2$  (diamonds in Fig. 16a) shows that there are no significant chemical differences among the three types of pumice (light-coloured, dark-grey and banded) or in the products of the three members. The primordial mantle-normalised multi-element diagram (Fig. 16b) reveals that the samples are compositionally homogenous and show Th, Sr and Ti negative anomalies and Zr positive anomaly.

By contrast, groundmass glass compositions (circles in Fig. 16a) are less homogeneous and more evolved than

whole-rock compositions. Major element concentrations in the groundmass glass reveal two different trends: light-coloured glass consistently shows higher contents of  $\text{TiO}_2$ , FeOt, MnO and MgO when compared with dark-grey glass. The dark-grey glass has higher contents of  $\text{Al}_2\text{O}_3$  and CaO that decrease with increasing  $\text{SiO}_2$ , while  $\text{K}_2\text{O}$  shows the opposite behaviour.

The concentration of residual volatile species (halogens and sulphur) in the two types of groundmass glass is also considerably different. The light-coloured glass has a higher concentration of  $\text{SO}_3$  ( $\leq 0.09$  wt%), while in the dark-grey glass, with the exception of one value of 0.03 wt%  $\text{SO}_3$ , it is below the detection limit of the electron microprobe. Chlorine concentrations range from 0.12 to 0.21 wt% in the light-coloured glass, but is always below the detection limit in the dark-grey glass.

Overall, the juvenile products of C11 show the same mineral assemblage and whole-rock compositions throughout the three members, indicating that the bulk magma composition remained constant during the eruption. However, the simultaneous presence of light-coloured, dark-grey and banded clasts (with different vesicularity and

**Table 5** Average C11 whole-rock pumice and groundmass glass composition. All values in weight percent

Oxides	Whole-rock <sup>a</sup>	Light-coloured glass	Dark-grey glass
No.	6 ( $\pm 1\sigma$ )	52 ( $\pm 1\sigma$ )	8 ( $\pm 1\sigma$ )
$\text{SiO}_2$	59.33 (0.27)	64.20 (0.99)	62.81 (2.41)
$\text{TiO}_2$	1.00 (0.02)	0.65 (0.10)	0.13 (0.06)
$\text{Al}_2\text{O}_3$	17.81 (0.23)	18.62 (0.27)	22.70 (2.18)
FeOt <sup>b</sup>	4.83 (0.07)	3.75 (0.29)	0.54 (0.19)
MnO	0.16 (0.00)	0.16 (0.03)	0.05 (0.03)
MgO	1.27 (0.08)	0.70 (0.16)	0.05 (0.03)
CaO	3.06 (0.04)	1.96 (0.39)	3.91 (2.17)
$\text{Na}_2\text{O}$	6.20 (0.06)	6.01 (0.33)	7.71 (0.48)
$\text{K}_2\text{O}$	3.76 (0.03)	4.22 (0.36)	2.33 (2.02)
$\text{P}_2\text{O}_5$	0.31 (0.02)	0.18 (0.06)	0.07 (0.05)
LOI	1.44 (0.46)	—	—
$\text{SO}_3$	—	0.04 (0.02)	0.03
Cl	—	0.16 (0.02)	—
Total	99.17	100.67	100.33

No. number of analyses

<sup>a</sup> Whole-rock composition of light-coloured, dark-grey and banded pumices

<sup>b</sup> Total Fe reported as FeOt (from whole-rock analyses  $\text{FeOt} = 0.8998 \times \text{Fe}_2\text{O}_3\text{t}$ )

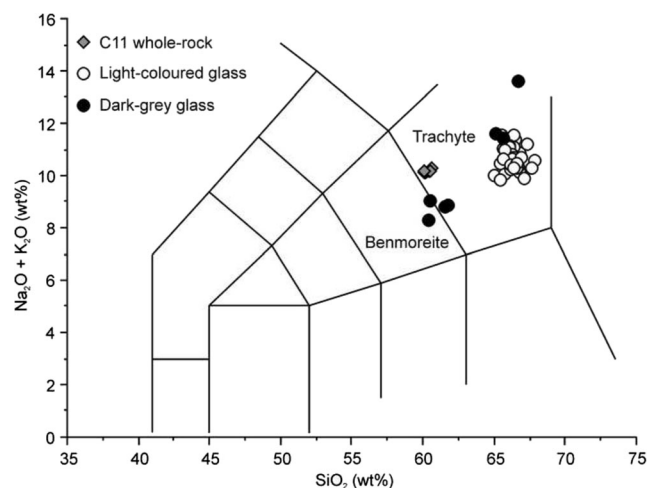


**Fig. 15** Total alkalis vs. silica (TAS) diagram (Le Bas et al. 1986) for the classification of C11 whole-rock pumice and groundmass glass

crystallinity), frequent disequilibrium features in phenocrysts, distinct groundmass glass compositions and residual volatile contents suggest the occurrence of magma mingling/mixing.

### Magmatic intensive parameters

The magmatic intensive parameters are constrained using the magnetite-ilmenite geothermometer of Andersen and Lindsley (1985) with Stormer (1983). Temperature and oxygen fugacity were obtained from coexisting microphenocrysts of magnetite and ilmenite set in groundmass and tested for equilibrium following Bacon and Hirschmann (1988). The equilibrium temperatures are in the range of 923–976 °C with oxygen fugacity values ( $\log f_{\text{O}_2}$ ) of  $-11.7$  to  $-10.5$  log units, close to the Ni-NiO oxygen buffer. These values are representative of pre-eruptive magmatic conditions along the upper part of the feeding system, due to the rapid re-equilibration timescales of coexisting Fe-Ti oxides (e.g. Gardner et al. 1995; Venezky and Rutherford 1999).

The presence of amphibole enables the estimation of magma storage conditions using the Ridolfi et al. (2010) geothermobarometer. Intensive parameter estimates yield a temperature range of 953–1040 °C and oxygen fugacity of  $-12.1$  to  $-10.3$   $\log f_{\text{O}_2}$ , near the Ni-NiO oxygen buffer. The estimated pressure varies between 290 and 510 MPa, which correspond to depths of 10 to 18 km. The water content of the melt in equilibrium with the amphibole is estimated at 3.3–5.2 wt%. However, as this algorithm only considers the composition of amphibole and does not account for re-equilibrium conditions with the melt or other mineral phases (e.g. Shane and Smith 2013), the calculated parameters refer to amphibole crystallisation conditions, which most likely record deeper magmatic conditions than those obtained by coexisting magnetite-ilmenite pairs.

Regardless of the different formulations of the geothermometers, the calculated parameters are in agreement between them and with those of Zanon et al. (2013), who estimated a magmatic temperature of  $953 \pm 22$  °C.

## Discussion

### Magma mingling/mixing

The ubiquitous presence of banded, light-coloured and dark-grey pumice clasts throughout the C11 deposit suggests the simultaneous eruption of two types of magmas. We propose that the dark-grey and light-coloured clasts represent distinct magma batches, although with similar bulk characteristics (whole-rock composition and mineral assemblage). This hypothesis is supported by the different textural features (vesicularity and crystallinity) and groundmass glass compositions (major elements and residual volatiles) which provide

evidence for the interaction of two magmas (e.g. Huppert et al. 1982; Clyne 1999; Tepley et al. 2000; Sosa-Ceballos et al. 2012). The dark-grey magma was slightly more differentiated and degassed than the light-coloured magma. This indicates that the two batches evolved independently from one another before mingling/mixing. The dark-grey magma was probably stored at a shallower level for a longer time, sufficient to exsolve volatiles and crystallise (e.g. Hammer and Rutherford 2002; Wright et al. 2011), while the light-coloured magma may have been stored at greater depth.

According to Zanon et al. (2013) and Zanon and Frezzotti (2013), the trachytic magmas erupted from Caldeira Volcano evolved through two-step fractional crystallisation starting at a depth of  $\sim 16$  km. The shallower level of differentiation, located at  $\sim 5$  km depth, is part of a complex magma storage system, composed of small independent reservoirs, that fed the various explosive eruptions (Dias et al. 2007).

Other deposits of the Cedros Volcanic Complex Upper Group (C4 and C9; Pacheco 2001; Zanon et al. 2013) also show banded pumice clasts with similar characteristics to those of C11, suggesting that magma mingling/mixing processes are common at Caldeira Volcano storage system.

We hypothesise that prior to the C11 eruption, the rising volatile-rich light-coloured magma encountered the more degassed and differentiated dark-grey magma. The volume and volatile influx from this interaction may have triggered the eruption.

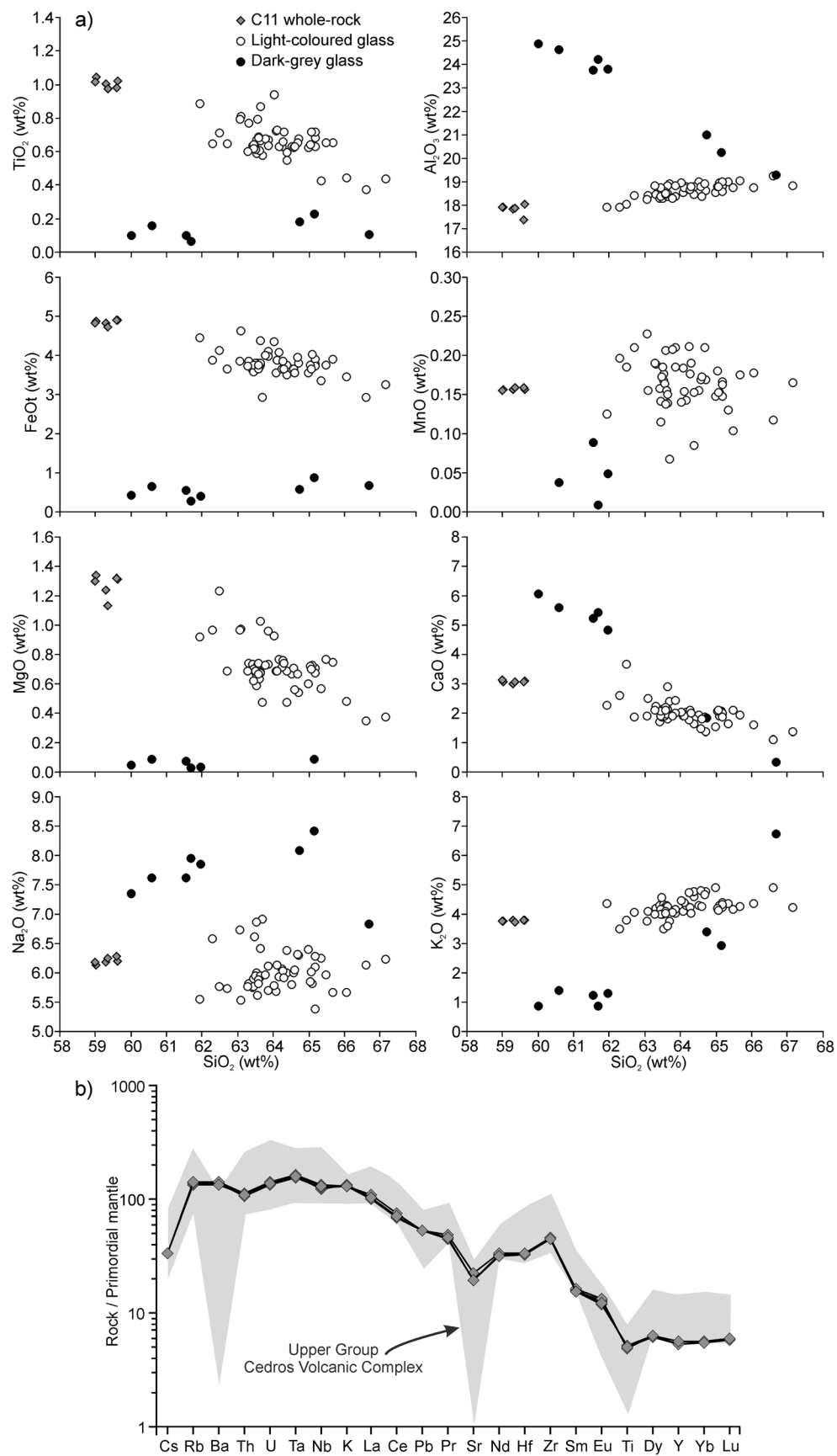
Although the two magmas have similar bulk compositions and mineral assemblages, the presence of banded clasts indicates that the mixing process was incomplete. In fact, macroscopically uniform coloured pumice clasts show micro-scale banding under the microscope. Therefore, the bulk composition of the C11 magma results from mingling and limited mixing of the two trachytic magma batches.

### Reconstruction of the eruption history

The C11 eruption was the last major explosive event at Caldeira Volcano. The magma involved ( $>0.1$  km<sup>3</sup> DRE) resulted from the mingling and partial mixing of two trachytic batches, which may have acted as the eruption trigger. The eruption had three main phases with distinct eruptive styles without major pauses in between (Fig. 17).

**Phreatomagmatic phase** The eruption started with a series of phreatomagmatic explosions as the ascending magma encountered a crater pond or an aquifer. These explosions produced short-lived eruption columns that deposited widespread ash fall layers (0.08 km<sup>3</sup> total bulk volume) on the NW sector of the island.

The phreatomagmatic phase was characterised by pulsating activity and formed unstable columns that alternated between



◀ **Fig. 16** **a** Variation diagrams for major elements (wt%) vs. SiO<sub>2</sub> (wt%) for C11 whole-rock pumice and groundmass glass. **b** Primordial mantle-normalised multi-element diagram (McDonough and Sun 1995) for C11 whole-rock. Six samples, including light-coloured, dark-grey and banded clasts, are plotted in the diagram; shaded area corresponds to the products of the Cedros Volcanic Complex Upper Group (Zanon et al. 2013)

convective and collapsing regimes (Fig. 17a). Partial or total column collapses produced single-pulse fully dilute PDCs.

During the course of the eruption, there was a change in the eruptive dynamics, as magmatic fragmentation became progressively more dominant. This led to the formation of quasi-sustained eruption columns that showered coarser grained ash and some pumice lapilli beds over the NW flank of the volcano.

**Sub-Plinian phase** After the initial phase, the eruption entered a fall-dominated phase characterised by magmatic fragmentation and the establishment of a sub-Plinian column up to 14 km high. It produced a coarse pumice fall deposit (0.07 km<sup>3</sup> total bulk volume), over the north flank as result of strong SSE-blowing winds (Fig. 17b). Ballistic trajectory transport was also significant in the overall dynamics of this phase.

The eruption column experienced minor unsteadiness, as it briefly waned, allowing the settling of residual ash suspended in the atmosphere, before waxing again to a sustained column. This phase was intense and short-lived, suggesting rapid draining of magma from the reservoir. This is supported by the increase in lithic clasts, such as hydrothermally altered clasts and syenite xenoliths, which indicates that the conduit was being eroded and widened to deeper levels of the volcanic system.

**PDC-dominated phase** During the final phase, the eruption was marked by a dramatic change in eruptive style characterised by the generation of widespread PDCs. As the conduit gradually became wider from continuous erosion, the eruption column became unstable shifting from a sustained sub-Plinian column to a collapsing column.

The eruptive dynamics were dominated by vigorous and prolonged pyroclastic fountaining that produced sustained quasi-steady PDCs (Fig. 17c). These deposited an ignimbrite sheet (0.07 km<sup>3</sup> preserved bulk volume on land) that reached the sea on the north and west sectors of the island. It is estimated that a large volume of material was deposited offshore.

As the magma was progressively withdrawn from the reservoir and the conduit wall eroded, the summit of Caldeira Volcano became unstable and collapsed. This is recorded by the marked increase in the abundance and size of lithic clasts and the subsequent deposition of lithic breccias. The eruption rapidly waned and ceased shortly after.

## Summit collapse and comparison with other eruptions

Based on the recent (<16 ka) stratigraphic record, the C11 eruption was a significant event in the eruptive history of Caldeira Volcano. All preceding and subsequent eruptions were characterised by small volume events which produced predominantly pumice and ash fall deposits (Pacheco 2001). By contrast, the final phase of the C11 eruption showed a remarkable change in eruptive style from sustained columns to prolonged pyroclastic fountaining, accompanied by significant erosion of the conduit wall and collapse of the summit, as recorded by the deposition of an extensive ignimbrite followed by lithic breccias.

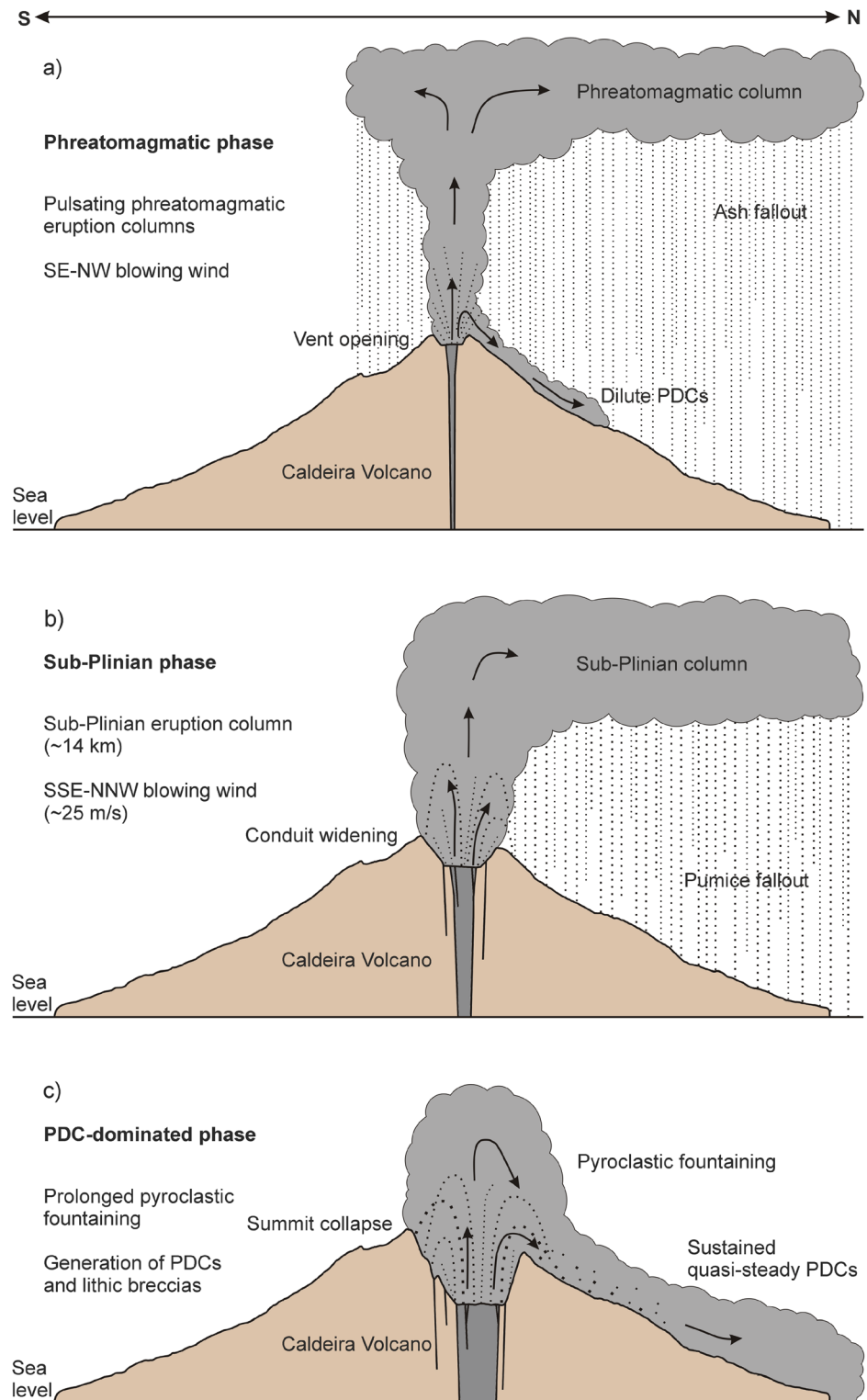
Although the total bulk volume of the C11 eruption is uncertain (due to the offshore deposition of material, especially from PDCs of the final phase), the amount of lithic clasts in the ignimbrite (up to 50 wt%) and in the lithic breccias is much less than the material missing from the top of the volcano. Moreover, Caldeira Volcano is crossed by WNW-ESE extensional faults, responsible for the down-faulting of the north sector of the summit (e.g. Madeira 1998; Tripanera et al. 2014; see Fig. 1b).

The evidence requires a summit collapse event to account for the 2-km-wide, ~370-m-deep void. We propose that the caldera was mostly formed during the final phase of C11, following the collapse of the summit into a cored-out central vent (e.g. Walker 1984; Scandone 1990). This collapse may have been favoured by the structural weakness associated with the extensional fault system crossing the volcano.

Little is known about the substructure of the caldera; however, its diameter and steep-sided morphology closely resemble those of funnel-type structures (e.g. Nigorikawa and Sunagohara calderas, Japan; Lipman 1997). These are associated with small volume explosive eruptions from central vents overlying small magmatic reservoirs (Lipman 1997; Acocella 2007), similar to that discussed in the case of the C11 eruption. The formation mechanisms of small calderas are still poorly understood. However, comparable size calderas (~2 km in diameter) are known to have formed, in historical times, from a wide range of eruptive styles: Miyakejima AD 2000, Japan (Geshi et al. 2002); Vesuvius AD 79, Italy (Carey and Sigurdsson 1987); or Pinatubo AD 1991, Philippines (Scott et al. 1996).

In the Azores, and in many cases around the world (e.g. Vulcini Volcanic District, Italy; Nappi et al. 1991), calderas are not single collapse structures formed during large CFEs, but rather formed incrementally by the coalescence of collapses during a series of intermediate to small volume explosive eruptions (e.g. Walker 1984; Guest et al. 1999; Queiroz et al. 2008; Gertisser et al. 2010). Given the relatively small size of these calderas (<5–6 km<sup>3</sup>) and the evidence that they grow incrementally by multiple explosive eruptions, single eruptive

**Fig. 17** Sketch showing a summary of the eruptive phases of the C11 eruption. **a** Phreatomagmatic phase. **b** Sub-Plinian phase. **c** PDC-dominated phase. Eruption columns and PDCs are not to scale



events of  $<1 \text{ km}^3$  DRE are probably the maximum volume eruptions (Gertisser et al. 2010). For example, the Fogo A ( $\sim 0.6 \text{ km}^3$  DRE; Walker and Croasdale 1971) and the Lajes-

Angra Ignimbrite ( $\sim 0.3 \text{ km}^3$  DRE; Self 1976) eruptions have been associated with caldera formation at Fogo and Pico Alto volcanoes, respectively.

The C11 eruption is here interpreted as the first stage of formation of an incremental caldera, through the development of a funnel-type structure. This incipient summit collapse marks a major change in the evolution of Caldeira Volcano (as seen in other volcanoes of Azores), following the fairly recent (<16 ka) transition from basaltic effusive volcanism to trachytic explosive activity.

## Conclusions

The C11 pyroclastic succession records the ~1000-years BP explosive eruption of Caldeira Volcano (Faial Island). This study provides a new understanding of the eruptive dynamics of complex explosive eruptions in small ocean islands. New field and laboratory data revealed that the C11 eruption was small in volume (at least 0.22 km<sup>3</sup> minimum bulk volume) but had a rather complex eruption history.

Overall, >0.1 km<sup>3</sup> DRE of trachytic magma was involved in the eruption. Pre-eruptive magmatic temperatures were 950 ± 27 °C, with oxygen fugacity of -11.1 ± 0.6 log units around the Ni-NiO oxygen buffer. The bulk magma composition is inferred to have resulted from the mingling and partial mixing of two trachytic magma batches with different degrees of evolution.

The initial phase of the eruption was characterised by pulsating phreatomagmatic explosions, producing short-lived eruption columns and occasional fully dilute PDCs. These deposited a sequence of parallel-bedded ash layers over the NW sector of Faial. The eruption continued to a more stable fall-dominated phase with the establishment of a ~14-km-high sub-Plinian column (peak MER of 1.2 × 10<sup>7</sup> kg/s) that deposited coarse pumice on the north flank of the volcano. The final phase was marked by prolonged pyroclastic fountaining and the generation of sustained quasi-steady PDCs, which deposited an ignimbrite sheet along the north and east flanks of the volcano. Conduit wall erosion and summit collapse is recorded by an increase in lithic clast abundance and by the deposition of lithic breccias.

The C11 eruption is thought to correspond to the first stage of incremental caldera formation. Compared with other CFEs in Azores and worldwide, C11 was a small event; however, another similar eruption would have a large impact on a small island like Faial (~170 km<sup>2</sup>).

These findings help to better understand complex explosive eruptions on ocean islands and provide a framework for assessing the volcanic hazards associated with this type of events on Faial and elsewhere.

**Acknowledgments** This work was funded by a Fundo Regional da Ciência e Tecnologia PhD scholarship to A. Pimentel (M3.1.2/F/022/2007) and partially supported by Fundação para a Ciência e Tecnologia (PTDC/CTE-GIX/098836/2008). Thanks to V. Zanon for the help with

the electron microprobe analyses and to M. Porreca for the field assistance. Further thanks go to A. Mendes for the help with the grain size analyses. The authors acknowledge G. Giordano, U. Kueppers, R. J. Brown and an anonymous reviewer for comments that significantly improved the manuscript.

## Appendix

### Grain size, component and morphologic analyses

Twenty-five samples were sieved at 0.5  $\phi$  intervals ( $\phi = -\log_2 d$ , where  $d$  is grain size on mm) in the range -6 to 5  $\phi$  (64–0.032 mm). Coarser grain sizes (-6 to -3  $\phi$ ) were gently hand-sieved in the field to avoid artificial breakage of pumice clasts and generation of fine ash by abrasion. The fractions were weighed to 0.1 g. Finer grain sizes (-2.5 to 5  $\phi$ ) were dried in an oven for 24 h and split into three subsamples of 100 cm<sup>3</sup>. Each batch was mechanically sieved and weighed to 0.0001 g. Grain size parameters of Inman (1952) and Folk and Ward (1957) were calculated. To facilitate comparison among different samples, fractions coarser than -6  $\phi$  were not considered.

Componentry analyses were carried out on selected samples. From -6 to -3  $\phi$ , the components were separated in the field into pumice and lithic clasts. Finer fractions, -2.5 to 1  $\phi$ , were separated in the laboratory with the naked eye or under a binocular microscope into pumice clasts, lithic clasts and crystals. For each size class, a minimum of 800 grains was separated and weighed to 0.0001 g.

Morphologic analysis of fine-grained ash particles was performed by scanning electron microscope (SEM) imaging. Prior to image acquisition, ash particles from six representative samples in the range between 4 and 5  $\phi$  were selected and mounted onto stubs. The images were acquired with a JEOL-5410 SEM, at the Departamento de Biologia/Centro de Investigação dos Recursos Naturais of the University of Azores (Portugal), operating at secondary electron mode with an acceleration voltage of 15 kV.

### Petrography, whole-rock geochemistry and mineral chemistry analyses

The petrographic features and modal analyses of eight unaltered pumice clasts were obtained by thin section observation. On each thin section, a minimum of 800 points was counted.

Whole-rock geochemical analyses of major and trace elements of six samples, representative of the juvenile products from the three members, were carried out at Activation Laboratories Ltd., Ontario (Canada) by lithium metaborate/tetraborate fusion inductively coupled plasma (FUS-ICP) and inductively coupled plasma mass spectrometry (ICP-MS) techniques (following code 4LITHO). Further information on the analytical methods is available at the Activation

Laboratories website ([www.actabs.com](http://www.actabs.com)). Reproducibility for major and trace elements is commonly assessed to be better than 10 %.

Electron microprobe analyses were performed on eight samples with a JEOL JXA 8200 Superprobe, at the Dipartimento di Scienze della Terra “Ardito Desio” of the University of Milan (Italy). A spot size of 1  $\mu\text{m}$  with a current of 15 nA was used for all mineral phases, except alkali feldspars (5  $\mu\text{m}$  spot size and 5 nA current). Groundmass glass was analysed with a  $\sim 10\text{-}\mu\text{m}$ -wide defocused beam and a current of 2–4 nA. Count times for major elements were 30 s on the peak and 10 s on each background. Typical detection limit for each element is 0.01 %.

## References

- Acocella V (2007) Understanding caldera structure and development: an overview of analogue models compared to natural calderas. *Earth-Sci Rev* 85:125–160
- Allen SR, Cas RAF (1998) Rhyolitic fallout and pyroclastic density current deposits from a phreatoplinian eruption in the eastern Aegean Sea, Greece. *J Volcanol Geotherm Res* 86:219–251
- Andersen DJ, Lindsley DH (1985) New (and final!) models for the Ti-magnetite/ilmenite geothermometer and oxygen barometer. *Eos* 66:416
- Bacon CR, Hirschmann MM (1988) Mg/Mn partitioning as a test for equilibrium between coexisting Fe-Ti oxides. *Am Mineral* 73:57–61
- Barberi F, Cioni R, Rosi M, Santacroce R, Sbrana A, Vecchi R (1989) Magmatic and phreatomagmatic phases in explosive eruptions of Vesuvius as deduced by grain-size and component analysis of the pyroclastic deposits. *J Volcanol Geotherm Res* 38:287–307
- Branney MJ, Kokelaar P (2002) Pyroclastic density currents and the sedimentation of ignimbrites. Geological Society London, Memoir 27:152 pp
- Brown RJ, Branney MJ (2004) Event-stratigraphy of a caldera-forming ignimbrite eruption on Tenerife: the 273 ka Poris Formation. *Bull Volcanol* 66:392–416
- Brown RJ, Branney MJ (2013) Internal flow variations and diachronous sedimentation within extensive, sustained, density-stratified pyroclastic density currents flowing down gentle slopes, as revealed by the internal architectures of ignimbrites on Tenerife. *Bull Volcanol* 75:727
- Brown RJ, Kokelaar BP, Branney MJ (2007) Widespread transport of pyroclastic density currents from a large silicic tuff ring: the Glaramara tuff, Scafell caldera, English Lake District, UK. *Sedimentology* 54:1163–1189
- Caniaux G (2012) L'ignimbrite de Cedros sur l'île de Faial (Açores, Portugal). *Açoreana* 10:491–521
- Carey S, Sigurdsson H (1987) Temporal variations in column height and magma discharge rate during the 79 AD eruption of Vesuvius. *Geol Soc Am Bull* 99:303–314
- Carey S, Sparks RSJ (1986) Quantitative models of the fallout and dispersal of tephra from volcanic eruption columns. *Bull Volcanol* 48:109–125
- Cas RAF, Wright JV (1987) Volcanic successions. Modern and ancient. Allen and Unwin, London
- Chovelon P (1982) Évolution volcano-tectonique des îles de Faial et de Pico, Archipel des Açores, Atlantique Nord. PhD thesis, Université de Paris-Sud
- Clynne MA (1999) A complex magma mixing origin for rocks erupted in 1915, Lassen Peak, California. *J Petrol* 40:105–132
- Cole PD, Calder ES, Sparks RSJ, Druitt TH, Young SR, Herd R, Harford C, Norton G, Robertson R (2002) Pyroclastic flow deposits formed during the 1996–99 eruption of Soufrière Hills Volcano, Montserrat, W. I. In: Druitt TH, Kokelaar BP (eds) The eruption of Soufrière Hills Volcano, Montserrat, from 1995 to 1999, vol 21, Geological Society of London, Memoir, pp 231–262
- Cole PD, Queiroz G, Wallenstein N, Gaspar JL, Duncan AM, Guest JE (1995) An historic subplinian/phreatomagmatic eruption: the 1630 AD eruption of Furnas volcano, São Miguel, Azores. *J Volcanol Geotherm Res* 69:117–135
- De Rita D, Giordano G, Esposito A, Fabbri M, Rodani S (2002) Large volume phreatomagmatic ignimbrites from the Colli Albani volcano (Middle Pleistocene, Italy). *J Volcanol Geotherm Res* 118:77–98
- Dellino P, La Volpe L (1995) Fragmentation versus transportation mechanisms in the pyroclastic sequence of Monte Pilato-Rocche Rosse (Lipari, Italy). *J Volcanol Geotherm Res* 64:211–231
- Di Chiara A, Speranza F, Porreca M, Pimentel A, D'Ajello Caracciolo F, Pacheco J (2014) Constraining chronology and time-space evolution of Holocene volcanic activity on the Capelo Peninsula (Faial Island, Azores): the paleomagnetic contribution. *Geol Soc Am Bull* 126:1164–1180
- Dias NA, Matias L, Lourenço N, Madeira J, Carrilho F, Gaspar JL (2007) Crustal seismic velocity structure near Faial and Pico islands (Azores), from local earthquake tomography. *Tectonophysics* 445:301–317
- Douillet GA, Pacheco DA, Kueppers U, Letort J, Tsang-Hin-Sun E, Bustillos J, Hall M, Ramón P, Dingwell DB (2013) Dune bedforms produced by dilute pyroclastic density currents from the August 2006 eruption of Tungurahua volcano, Ecuador. *Bull Volcanol* 75:762
- Féraud G, Kaneoka I, Allègre CJ (1980) K/Ar ages and stress pattern in the Azores: geodynamic implications. *Earth Planet Sci Lett* 46:275–286
- Fierstein J, Nathenson M (1992) Another look at the calculation of fallout tephra volumes. *Bull Volcanol* 54:156–167
- Folk RL, Ward WC (1957) Brazos River bar: a study in the significance of grain size parameters. *J Sediment Petrol* 27:3–26
- Gardner JE, Rutherford M, Carey S, Sigurdsson H (1995) Experimental constraints on pre-eruptive water contents and changing magma storage prior to explosive eruptions of Mount St Helens volcano. *Bull Volcanol* 57:1–17
- Gente P, Dymont J, Maia M, Goslin J (2003) Interaction between the Mid-Atlantic Ridge and the Azores hot spot during the last 85 Myr: emplacement and rifting of the hot spot-derived plateaus. *Geochem Geophys Geosy* 4:8514
- Georgen JE, Sankar RD (2010) Effects of ridge geometry on mantle dynamics in an oceanic triple junction region: implications for the Azores Plateau. *Earth Planet Sci Lett* 298:23–34
- Gertisser R, Self S, Gaspar JL, Kelley SP, Pimentel A, Eikenberg J, Barry TL, Pacheco JM, Queiroz G, Vespa M (2010) Ignimbrite stratigraphy and chronology on Terceira Island, Azores. In: Groppelli G, Viereck-Goette L (eds) Stratigraphy and geology of volcanic areas. Geological Society of America, Special Paper 464, pp 133–154
- Geshi N, Shimano T, Chiba T, Nakada S (2002) Caldera collapse during the 2000 eruption of Miyakejima Volcano, Japan. *Bull Volcanol* 64:55–68
- Giordano G, De Rita D, Cas R, Rodani S (2002) Valley pond and ignimbrite veneer deposits in the small-volume phreatomagmatic ‘Peperino Albano’ basic ignimbrite, Lago Albano maar, Colli Albani volcano, Italy: influence of topography. *J Volcanol Geotherm Res* 118:131–144
- Guest J, Gaspar JL, Cole PD, Queiroz G, Duncan AM, Wallenstein N, Ferreira T, Pacheco JM (1999) Volcanic geology of Furnas Volcano, São Miguel, Azores. *J Volcanol Geotherm Res* 92:1–29

- Hammer JE, Rutherford MJ (2002) An experimental study of the kinetics of decompression-induced crystallization in silicic melt. *J Geophys Res* 107:148–227
- Hildenbrand A, Marques FO, Costa ACG, Sibrant ALR, Silva PF, Henry B, Miranda JM, Madureira P (2012) Reconstructing the architectural evolution of volcanic islands from combined K/Ar, morphologic, tectonic, and magnetic data: the Faial Island example (Azores). *J Volcanol Geotherm Res* 241–242:39–48
- Huppert HE, Sparks RSJ, Turner JS (1982) Effects of volatiles on mixing in calc-alkaline magma systems. *Nature* 297:554–557
- Inman DL (1952) Measures for describing the size distribution of sediments. *J Sediment Petrol* 22:125–145
- Le Bas MJ, Le Maitre RW, Streckeis A, Zanettin B (1986) A chemical classification of volcanic rocks based on the total alkali-silica diagram. *J Petrol* 27:745–750
- Lipman PW (1997) Subsidence of ash-flow calderas: relation to caldera size and magma-chamber geometry. *Bull Volcanol* 59:198–218
- Madeira J (1998) Estudos de neotectónica nas ilhas do Faial, Pico e S. Jorge: uma contribuição para o conhecimento geodinâmico da junção tripla dos Açores. PhD thesis, Universidade de Lisboa
- Madeira J, Brum da Silveira A (2003) Active tectonics and first paleoseismological results in Faial, Pico and S. Jorge Islands (Azores, Portugal). *Ann Geophys-Italy* 46:733–761
- Mason BG, Pyle DM, Oppenheimer C (2004) The size and frequency of the largest explosive eruptions on Earth. *Bull Volcanol* 66:735–748
- McDonough WF, Sun SS (1995) The composition of the Earth. *Chem Geol* 120:223–253
- Nappi G, Renzulli A, Santi P (1991) Evidence of incremental growth in the Vulsinian calderas (central Italy). *J Volcanol Geotherm Res* 47:13–31
- Newhall CG, Self S (1982) The volcanic explosivity index (VEI): an estimate of explosive magnitude for historical volcanism. *J Geophys Res* 87:1231–1238
- Pacheco JM (2001) Processos associados ao desenvolvimento de erupções vulcânicas hidromagmáticas explosivas na ilha do Faial e sua interpretação numa perspectiva de avaliação do hazard e minimização do risco. PhD thesis, Universidade dos Açores
- Pardo N, Macias JL, Giordano G, Cianfarra P, Avellán DR, Bellatreccia F (2009) The ~1245 yr BP Asososca maar eruption: the youngest event along the Nejapa-Miraflores volcanic fault, Western Managua, Nicaragua. *J Volcanol Geotherm Res* 184:292–312
- Pyle DM (1989) The thickness, volume and grain size of tephra fall deposits. *Bull Volcanol* 51:1–15
- Pyle DM (2000) Sizes of volcanic eruptions. In: Sigurdsson H, Houghton BF, McNutt SR, Rymer H, Stix J (eds) *Encyclopedia of volcanoes*. Academic, San Diego, pp 263–269
- Queiroz G, Pacheco JM, Gaspar JL, Aspinall WP, Guest JE, Ferreira T (2008) The last 5000 years of activity at Sete Cidades volcano (São Miguel Island, Azores): implications for hazard assessment. *J Volcanol Geotherm Res* 178:562–573
- Rampino MR, Self S (1982) Historic eruptions in Tambora (1815), Krakatau (1883), and Agung (1963), their stratospheric aerosols, and climatic impact. *Quaternary Res* 18:127–143
- Ridolfi F, Renzulli A, Puerini M (2010) Stability and chemical equilibrium of amphibole in calc-alkaline magmas: an overview, new thermobarometric formulations and application to subduction-related volcanoes. *Contrib Mineral Petr* 160:45–66
- Sahetapy-Engel S, Self S, Carey RJ, Naim IA (2014) Deposition and generation of multiple widespread fall units from the c. AD 1314 Kaharoa rhyolitic eruption, Tarawera, New Zealand. *Bull Volcanol* 76:836
- Scandone R (1990) Chaotic collapse of calderas. *J Volcanol Geotherm Res* 42:285–302
- Scott WE, Hoblitt RP, Torres RC, Self S, Martinez MML, Nillos T (1996) Pyroclastic flows of the June 15, 1991, climactic eruption of Mount Pinatubo. In: Newhall CG, Punongbayan RS (eds) *Fire and mud: eruptions and lahars of Mount Pinatubo, Philippines*. PHIVOLCS, Quezon City, pp 545–570
- Self S (1976) The recent volcanology of Terceira, Azores. *J Geol Soc London* 132:645–666
- Self S (2006) The effects and consequences of very large explosive volcanic eruptions. *Phil Trans R Soc A* 364:2073–2097
- Serralheiro A, Forjaz VH, Matos Alves CA, Rodrigues B (1989) Carta vulcanológica dos Açores – Ilha do Faial, escala 1:15.000. Serviço Regional de Protecção Civil, Universidade dos Açores, Centro de Vulcanologia INIC (eds), Ponta Delgada, 4 sheets
- Shane P, Smith VC (2013) Using amphibole crystals to reconstruct magma storage temperatures and pressures for the post-caldera collapse volcanism at Okataina volcano. *Lithos* 156–159:159–170
- Sohn YK, Chough SK (1989) Depositional processes of the Suwolbong tuff ring, Cheju Island (Korea). *Sedimentology* 36:837–855
- Sosa-Ceballos G, Gardner JE, Siebe C, Macias JL (2012) A caldera-forming eruption ~14,100 <sup>14</sup>C yr BP at Popocatepetl volcano, México: insights from eruption dynamics and magma mixing. *J Volcanol Geotherm Res* 231–214:27–40
- Stormer JC Jr (1983) The effects of recalculation on estimates of temperature and oxygen fugacity from analyses of multi-component iron-titanium oxides. *Am Mineral* 68:586–594
- Sulpizio R (2005) Three empirical methods for the calculation of distal volume of tephra-fall deposits. *J Volcanol Geotherm Res* 145:315–336
- Sulpizio R, Bonasia R, Dellino P, Mele D, Di Vito MA, La Voipe L (2010) The Pomici di Avellino eruption of Somma-Vesuvius (3.9 ka BP). Part II: sedimentology and physical volcanology of pyroclastic density current deposits. *Bull Volcanol* 72:559–577
- Sulpizio R, Dellino P (2008) Sedimentology, depositional mechanisms and pulsating behaviour of pyroclastic density currents. In: Gottsman J, Marti J (eds) *Caldera volcanism: analysis, modelling, and response*, vol 10, *Developments in volcanology*. Elsevier, Amsterdam, pp 57–96
- Sulpizio R, Mele D, Dellino P, La Volpe L (2007) Deposits and physical properties of pyroclastic density currents during complex Subplinian eruptions: the AD 472 (Pollena) eruption of Somma-Vesuvius, Italy. *Sedimentology* 54:607–635
- Tanguy J-C, Ribière C, Scarth A, Tjetjep WS (1998) Victims of volcanic eruptions: a revised data base. *Bull Volcanol* 60:137–144
- Tepley FJ III, Davidson JP, Tilling RI, Arth JG (2000) Magma mixing, recharge and eruption histories recorded in plagioclase phenocrysts from El Chichón Volcano, Mexico. *J Petrol* 41:1397–1411
- Tripanera D, Porreca M, Ruch J, Pimentel A, Acocella V, Pacheco J, Salvatore M (2014) Relationships between tectonics and magmatism in a transtensive/transform setting: an example from Faial Island (Azores, Portugal). *Geol Soc Am Bull* 126:164–181
- Venezky DY, Rutherford MJ (1999) Petrology and Fe-Ti oxide reequilibration of the 1991 Mount Unzen mixed magma. *J Volcanol Geotherm Res* 89:213–230
- Vogt PR, Jung WY (2004) The Terceira Rift as a hyper-slow, hotspot-dominated oblique spreading axis: a comparison with other slow-spreading plate boundaries. *Earth Planet Sci Lett* 218:77–90
- Walker G, Croasdale R (1971) Two Plinian-type eruptions in the Azores. *J Geol Soc London* 127:17–55
- Walker GPL (1981) Plinian eruptions and their products. *Bull Volcanol* 44:223–224
- Walker GPL (1984) Downsag calderas, ring faults, caldera sizes, and incremental caldera growth. *J Geophys Res* 89:8407–8416
- Wallenstein N (1999) Estudo de história recente e do comportamento eruptivo do Vulcão do Fogo (S. Miguel, Açores). Avaliação preliminar do hazard. PhD thesis, Universidade dos Açores
- Wilson CJN (1985) The Taupo eruption, New Zealand II. The Taupo ignimbrite. *Phil Trans R Soc A* 314:229–310

- Wilson L, Walker GPL (1987) Explosive volcanic-eruptions—VI. Ejecta dispersal in Plinian eruptions: the control of eruption conditions and atmospheric properties. *Geophys J Roy Astr S* 89:651–679
- Wohletz KH (1983) Mechanisms of hydrovolcanic pyroclast formation: grain-size, scanning electron microscopy, and experimental studies. *J Volcanol Geotherm Res* 17:31–63
- Wright HMN, Folkes CB, Cas RAF, Cashman KV (2011) Heterogeneous pumice populations in the 2.08-Ma Cerro Galán Ignimbrite: implications for magma recharge and ascent preceding a large-volume silicic eruption. *Bull Volcanol* 73:1513–1533
- Zanon V, Frezzotti ML (2013) Magma storage and ascent conditions beneath Pico and Faial islands (Azores Islands): a study on fluid inclusions. *Geochem Geophys Geosy* 14:3494–3514
- Zanon V, Kueppers U, Pacheco JM, Cruz I (2013) Volcanism from fissure zones and central volcanoes: geochemical processes in multiple feeding systems. The case study of Faial Island - Azores archipelago. *Geol Mag* 150:536–555